ABSTRACT

Title of thesis: PROBING BIOPHYSICAL PROPERTIES OF THERAPEUTIC PROTEIN AGGREGATES WITH INTERFEROMETRIC SCATTERING MICROSCOPY

Nathan Augustus Wong, Master of Science, 2021

Thesis directed by: Professor Taylor J. Woehl
Department of Chemical and Biomolecular Engineering

A growing biopharmaceutical market increases the importance of therapeutic proteins, of which monoclonal antibodies (mAb) are the largest category. Protein aggregation in biopharmaceutical production has important consequences in mAb immunogenicity. Submicron (100-1000 nm) protein aggregates in particular are a key challenge due to their higher immunogenicity and the relative lack of analytical methods capable of characterizing them. We propose the use of interferometric scattering (IFS) microscopy as a simple and potentially high-throughput orthogonal characterization method of submicron aggregates. We demonstrate its utility by testing two variants of IFS microscopy: (1) Correlative IFS and fluorescence microscopy (2) hyperspectral interferometric scattering (h-IFS) microscopy. Using correlative IFS and fluorescence microscopy, we characterize the size and surface structure of a stirred protein aggregate sample. We find that smaller protein aggregates (~100 nm) have higher surface concentrations of Fc domains and hydrophobic regions. Then, we demonstrate the usage of h-IFS microscopy to differentiate and quantify protein aggregates and contaminants in biologic drugs.

PROBING BIOPHYSICAL PROPERTIES OF THERAPEUTIC PROTEIN AGGREGATES WITH INTERFEROMETRIC SCATTERING MICROSCOPY

by

Nathan Augustus Wong

Thesis submitted to the Faculty of the Graduate School of the
University of Maryland, College Park, in partial fulfillment
of the requirements for the degree of
Master of Science
2021

Advisory Committee:

Professor Taylor J Woehl, Chair
Professor Jeffery B. Klauda
Professor Ganesh Sriram

Dedication

I dedicate this thesis to my family and friends who have all given a world of support, and especially to my late father who encouraged and inspired me to study chemical engineering.

Acknowledgement

First and foremost, I thank my advisor Dr. Taylor Woehl his endless support, without which I would not have been able to finish my degree program. I am grateful for everything you have done for me throughout my entire time in your lab group. I would also like to thank Dr. Jeffrey Klauda and Dr. Ganesh Sriram, for graciously offering their time to join my committee. To all the members of the Woehl lab group, thank you for all the help over the years. I especially thank the other graduate students for their mentorship, thank you Mei, Shakiba, and Umesha. Lastly, a final thank you to Dr. Deborah Goldberg for helping me through a difficult period.

Table of Contents

List of Tables

List of Figures

Chapter 1: Introduction

1.1 Monoclonal Antibodies in the Biopharmaceutical Industry

Therapeutic monoclonal antibodies (mAb) are engineered antibodies designed to treat diseases by binding to specific drug targets in the body with high specificity. A mAb comprises identical antibodies all cloned from a single B-lymphocyte parent, and each will target the same kind of substance. The advantage of monoclonal antibodies is their ability to selectively target disease-causing substances, significantly increasing efficacy and reducing side effects over non-targeted drugs. Their importance to the biopharmaceutical industry is such that monoclonal antibodies are by far the largest category of drugs. Since the first FDA approved mAb was introduced to the market in 1986, a total of 139 mAb drugs have since been approved in the US and Europe.[1,2] Of those 139 approved mAbs, more than 75% were introduced between 2010 and 2019 due to rapid recent growth in the market as well as advances in research and development. Global sales revenue of mAbs has increased from $75 billion to $163 billion between 2013 to 2019, which accounts for more than 70% of all biopharmaceutical sales.[3] Included in these sales numbers are related biopharmaceutical products derived from monoclonal antibodies such as mAb conjugates and fragments. Taken all together, mAb-related biopharmaceuticals are projected to continue to show strong economic growth.

In the human immune system, antibodies are produced by B cells after they have identified foreign material called antigens. Although there are several subclasses of antibodies, the primary one involved in the immune system is immunoglobulin G (IgG), shown in Figure 1.1. These antibodies specifically recognize and bind to those exact

types of antigens, which then leads to neutralization by various mechanisms. Antibodies are able to distinguish between foreign and native substances by the presence of molecular surface structures known as epitopes. Structurally, IgG antibodies are a Y-shaped protein comprising two identical chains known as the light and heavy chains. The two main sections of an IgG antibody are the variable region and the constant region, these two sections are broadly defined by their function. The fragment antibody binding (Fab) domains of the antibody's variable region are responsible for antigen binding, and the fragment crystallizable (Fc) region of the antibody's constant region is responsible for modulating the immune response. Recognition and binding to epitopes occur at the antigen binding sites, which are located at the ends of the light and heavy chains in the variable region.[4]

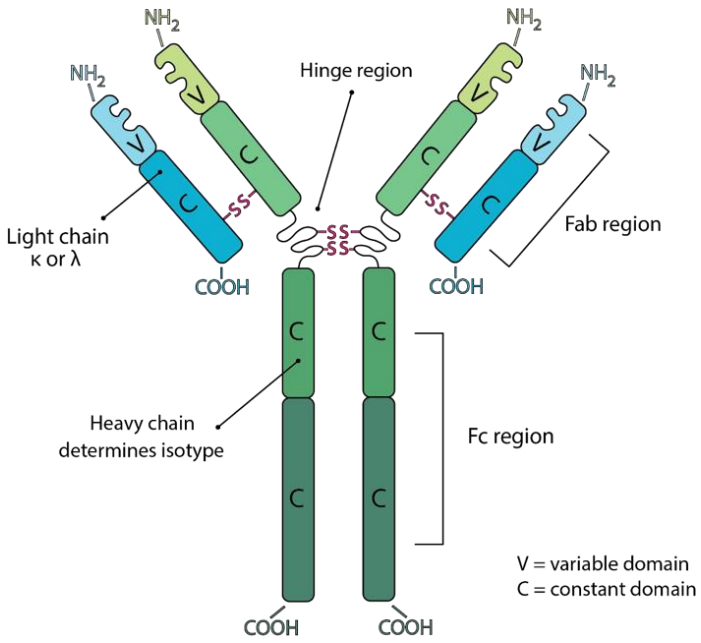

Figure 1.1. Diagram of an IgG antibody with variable region domains marked as "V" and constant region domains marked as "C". Disulfide bonds linking the light and heavy chains marked "SS". Reproduced with permission from Bxcell[5].

To allow binding to different kinds of antigens, the amino acid sequence at the antigen binding site is highly variable. The complementarity-determining region (CDR) is the specific area of the antigen binding site responsible for antigen recognition and binding.[6] On the other side of the constant region, the Fc region mediates the appropriate immune response after the antibody has bound to an antigen. Other cells involved in the immune response like macrophages and natural killer cells directly interact with the Fc region via Fc receptors located on their surface. For example, the antibody-dependent cellular toxicity response directly recruits natural killer cells to lyse antigens that have been bound by antibodies and have formed an antigen-antibody complex.[7] Due to its function in binding other immune system cells, the amino acid sequence of the constant region is highly conserved.

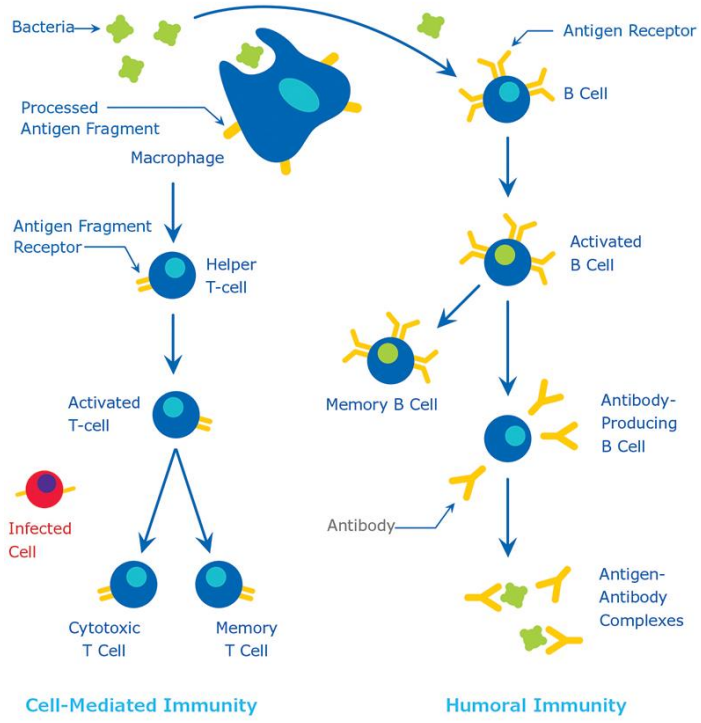

Figure 1.2. Schematic of an IgG antibody's role in the humoral immune response. Reproduced with permission from Sigma-Aldrich[8].

Prior to the development of monoclonal antibodies, only polyclonal antibodies (pAb) were available. Polyclonal antibodies are produced from different B cells, and will bind to different epitopes of the same antigen. Due to their variable binding properties, pAbs are unsuitable for therapeutic use. In 1975, the first mAbs were produced by hybridoma technology, which combined an antibody-producing B cell with immortal myeloma cell lines.[9,10] The resulting group of hybrids produced polyclonal antibodies, which were further screened and separated to produce large quantities of monoclonal antibodies. However, the B cells used for early hybridoma production were extracted from mice immunized against a certain epitope, and its use in therapeutics resulted in rejection by the human immune system.[11] The first mAb drug approved by the FDA in 1986 was muromonab-CD3. It was designed to reduce rejection of organ transplants, but caused numerous side effects due to being derived from mice. Patients who used the muromonab-CD3 developed antidrug antibodies (ADA) which targeted the drug and reduced efficacy.[9] In order to prevent immune system rejection, later mAbs took advantage of genetic engineering techniques developed in the 80s and 90s to produce chimeric mouse-human antibodies. The variable region sequences responsible for antigen binding were still derived from mice, but human sequences were substituted into the constant region to reduce rejection. Even more advanced humanization techniques resulted in only keeping the CDR sequences from the mice, and replacing the rest of the antibody sequences with human ones. Now, the newest mAbs are completely human-derived, with much lower rates of ADA responses.[10]

Given a specific substance of interest, an antibody targeting that substance can be obtained either through hybridoma technology or *in vitro* methods like phage display.[12]

Once obtained, the antibody's gene sequence is transfected into mammalian cell lines for growth and further screening. The most commonly used are Chinese hamster ovary cell lines, although mice and human cell lines are also used. Screening for clone selection aims for optimizing factors such as high protein production and cell growth. The tested clones are fed nutrients and grown in successively larger lab-scale tube cultures and bioreactors to simulate real manufacturing conditions and analyzed for productivity and quality. Some examples of monitored quality attributes are amino acid sequence mutation level, post-translational glycosylation level, and degree of aggregation. After screening and analysis, the top-performing clone is selected based on the above factors as well as its phenotypic stability, which is its ability to maintain consistent cell growth and product quality as the clones continue dividing.[13]

The manufacturing process is divided into upstream and downstream processes, as shown in Figure 1.3. Everything related to the growing of cells and production of antibodies is in the upstream process, and everything related to the harvest and purification of the antibodies belongs to the downstream process.

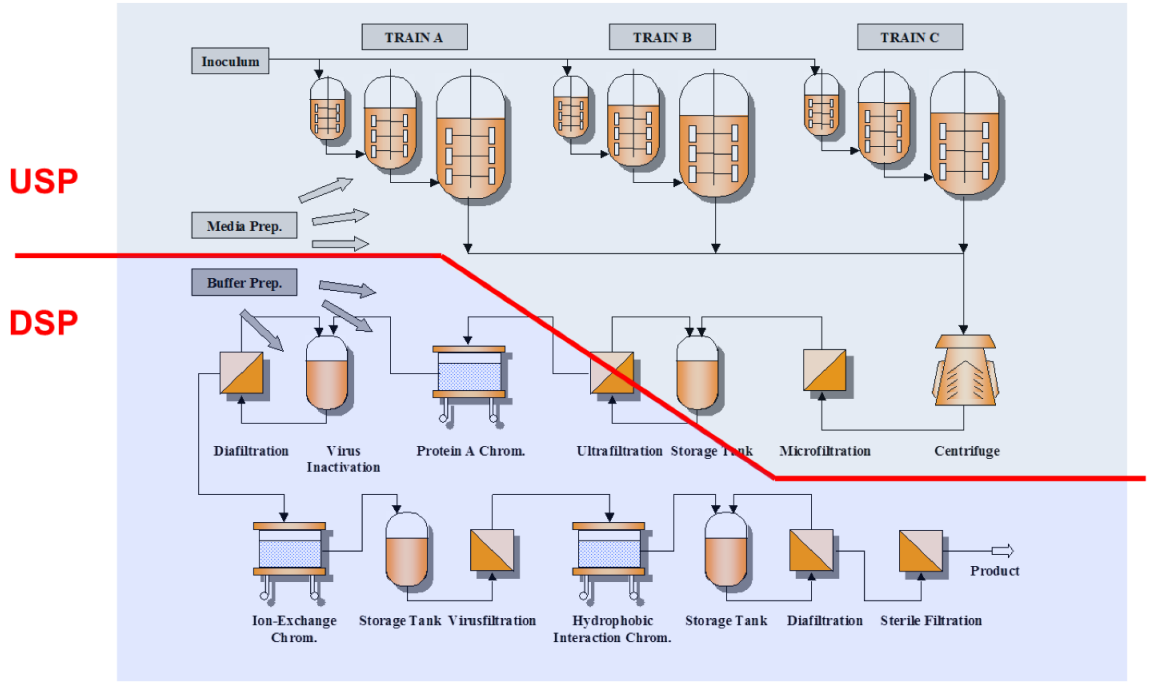

Figure 1.3. Schematic of upstream (USP) and downstream (DSP) processes involved in the production of therapeutic mAbs. Reproduced with permission from Gronemeyer[13].

Similar to clone screening, full-scale manufacturing is carried out in steps as cells grow and divide. Starting from small shake flasks, the contents are transferred to larger volumes once the available nutrients are exhausted. When the cell culture has grown sufficiently, it will be used to seed production in full-size bioreactors with continuous monitoring of nutrient levels and culture conditions such as temperature and pH levels.[14] Finally, once the upstream process has ended, which can take between several weeks and in excess of a month, the mAb product will be harvested from the contents of the bioreactor. After the bioreactor has finished running, it does not just contain the produced antibodies. There are also DNA fragments and other proteins from the host-cell, viruses, as well as antibody aggregates and fragments unsuitable for the final drug. The antibody must be separated and purified through a series of centrifugation, filtration, and

chromatography steps. Finally, the purified mAb product is packaged in a specially designed formulation made for maximizing shelf life and stability. If improperly stored, the mAb drug could experience early degradation before its shelf life ends.[15] The various forms of protein degradation are classified as either chemical degradation or physical degradation. Examples of chemical degradation include oxidation and deamidation, and examples of physical degradation are fragmentation and aggregation.[16]

1.2 Monoclonal Antibody Aggregates and Immunogenicity

Monoclonal antibody aggregation is of special interest because of the known immunogenicity of protein aggregates.[17] There are several formation pathways for protein aggregation, including reversible and irreversible aggregation. The primary formation pathway is initiated by partial unfolding of the monomer causing exposure of internal residues.[18] Protein aggregation immunogenicity has been shown to cause reduced drug efficacy due to production of anti-drug antibodies. In severe cases, immunogenic aggregates can also lead to development of diseases such as pure red cell aplasia via neutralization of endogenous proteins.[19] Protein aggregates range in size from small oligomers to visible aggregates with sizes of hundreds of microns.[20] The three size categories are: visible particles greater than 100 µm, subvisible particles between 100 nm and 100 µm, and oligomers between 10 nm and 100 nm.[20] An additional distinction is made for subvisible particles between 100 nm and 1µm, called submicron particles. Submicron particles in particular have been shown to be more immunogenic than other size classes, due to their large surface area to volume ratio.[21]

During production and storage, antibodies are exposed to various external stresses that induce aggregation such as low pH, high temperatures, agitation, and freeze-thaw cycles. Aggregates produced during production are removed with chromatography methods such as size exclusion chromatography (SEC) and cation exchange chromatography.[21] Furthermore, the addition of stabilizing excipients like sugars and surfactants to the drug formulation are meant to reduce degradation during storage. Despite these measures, post-production mishandling of biologics causes degradation that can increase clinical risk and decrease efficacy of those drugs. In hospital settings, it is common for biologics to encounter UV light exposure and temperatures outside the recommended storage range for extended periods. Routine handling of biologics leads to mechanical stresses such as shaking, dropping, and IV bag infusion.[22] Recent surveys of health worker and patient habits have revealed frequent mishandling of biologics due to lack of knowledge of their stability conditions.[23] Vlieland et al. found that only 6.7% of 225 patients kept their biologics at the correct storage temperature.[24]

Before a mAb is approved, immunogenicity is one attribute that is monitored during clinical trials. However, scaling up to commercial production can result in unforeseen aggregation due to changes between the lab-scale and full-scale processes. The FDA has established guidelines to characterize and limit subvisible particle levels in therapeutics; there should be no more than 6000 particles per vial with size ≥10 μm, and no more than 600 particles per vial with size ≥25 μm.[17] However as Carpenter et al. warns, these limits are based on the risk of blood vessel occlusion and not on immunogenicity factors.[16]

1.2.1 Aggregation Kinetics

Aggregation is a long-term protein degradation mechanism that depends on thermodynamic stability of the monomer's native state. Certain process conditions during monoclonal antibody production, such as low pH and high temperatures, can lead to lower native state stability and promote faster aggregation.[25] The thermodynamic and kinetic factors driving mAb aggregation can be better understood through mathematical models and experimental data. There are existing models that have been used for interpreting thermodynamic and kinetic data of protein degradation as it relates to neurodegenerative diseases such as Alzheimer's and Parkinson's disease. One model that has been adapted for mAb aggregation is the Lumry-Eyring model, which treats aggregation as a two-step process.[26] The first step is the reversible conformation changes of the monomer to a reactive unfolded state, followed by irreversible aggregation of the unfolded proteins. The later developed extended Lumry-Eyring model (ELE) better incorporated aggregation kinetics by making a distinction between different oligomer sizes. Instead of a two-step process, the ELE model has multiple steps taking into account the different rate constants of monomer-oligomer and oligomer-oligomer aggregation. Another modified form is the Lumry-Eyring nucleated polymerization (LENP) model (Figure 1.4), which adds a nucleation step and aggregate condensation step.[27,28]

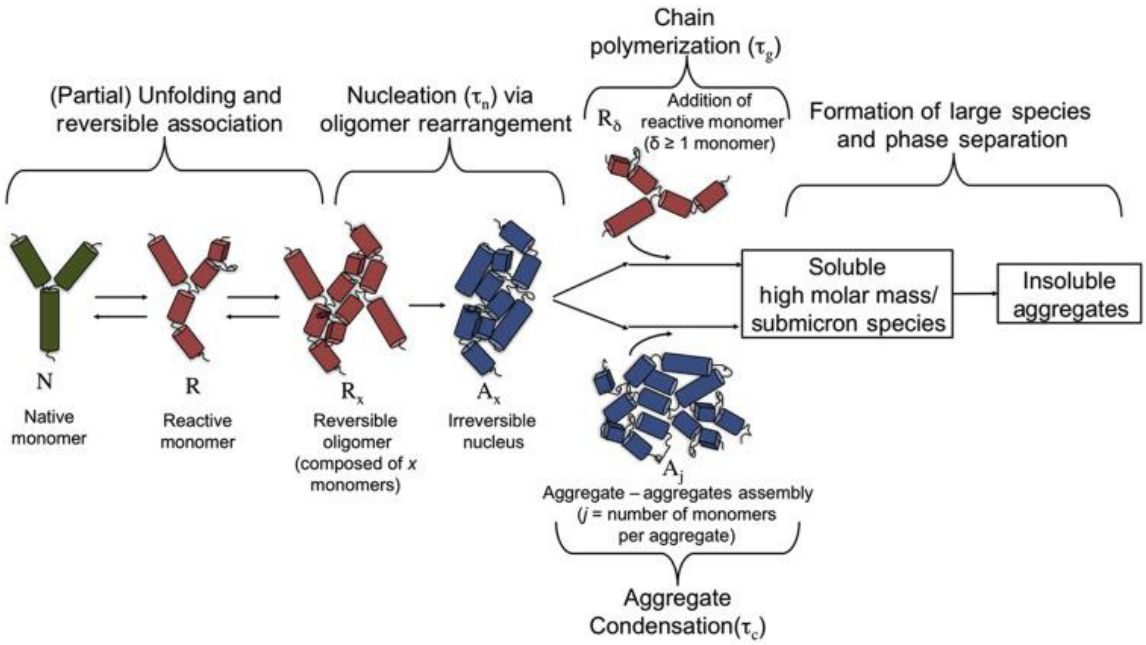

Figure 1.4. Aggregation process represented in the LENP model which includes a nucleation step. Reproduced with permission from Bria[27].

Compared to the ELE model, the LENP model has been shown to more accurately describe IgG1 mAb aggregation kinetics over a range of experimental conditions. Using both models, Singla et al. showed that pH plays the largest role in aggregation, followed by temperature, ionic concentration, and buffer type.[26] Their results across different conditions indicated that nucleation is important to the aggregation process, which is likely why the LENP model was more accurately fitted.

1.2.2 Immunogenicity

Compared to aggregate formation kinetics, the mechanisms by which protein aggregates induce immunogenic reactions are less understood. It is thought that protein aggregates with some degree of their monomeric native structure preserved are more immunogenic than more denatured proteins.[29] Because of their high surface area to

volume ratio, subvisible particles in particular have higher immunogenic potential, which has been demonstrated by higher ADA production after subcutaneous injection of protein aggregates in murine models.[21, 30] Due to their repetitive structure, protein aggregates are structurally similar to pathogen epitopes that are recognized by the immune system. One hypothesis is that protein aggregates are captured by antigen presenting cells (APC) such as B-cells and macrophages, which leads to formation of ADAs against the mAb monomer.[30] There are few reports combining clinical cases of immunogenicity and administered drug characteristics. Thus, specifically linking aggregation levels and clinical immunogenicity examples is difficult. One of the few documented cases is recombinant erythropoietin, used to treat anemia. In Europe, changes to the drug formulation to include a surfactant and swapping from vials to syringes led to cases of pure red blood cell aplasia.[19] It was determined that increased aggregation levels resulting from the change in formulation and delivery method led to cross-reactions with the endogenous erythropoietin and formation of ADAs. Monoclonal antibody aggregates have also been shown to be capable of direct activation of Fcγ receptors, triggering immune responses such as activation of inflammatory cytokines.[31] Thus, it is possible that protein aggregate immunogenicity is affected by surface attributes not easily characterized in the submicron particle range.

1.3 Overview of Protein Aggregate Characterization Methods

There are multiple characterization methods of protein aggregates that operate on different principles and cover different size ranges. Analysis of visible particles is frequently done by visual inspection, also using techniques like light obscuration, and is

generally simple to perform but is not an exact measurement. Oligomers in particular are well-characterized by methods such as size exclusion chromatography (SEC) and gel electrophoresis.[32] However, there are fewer characterization methods capable of investigating subvisible particles and the existing ones are generally limited by low throughput and robustness. More specifically, there are a lack of quantitative methods for measuring the concentration and size distribution of submicron particles with sizes ranging from 100 nm – 1 μm.[33] Thus, it is important to focus efforts on developing novel characterization methods with potential for quality control and better understanding of protein aggregates.

1.3.1 Size Exclusion Chromatography

Size exclusion chromatography is a method of separating particles based on size, but can also be used to detect and measure protein aggregate quantities. It is suitable for proteins and aggregates sized between 1-100 nm.[34] A column is packed such that the matrix pore sizes exclude any particles over a certain size and shape, and any particle smaller will elute through the column quicker. Elution time increases with particle size. A calibration curve can be used to measure molecular weight based on elution time. However, the calibration curve is based on well-characterized proteins that may differ from the protein aggregates of interest that may have irregular shapes and post-translational modifications.[32] SEC separation can also be combined with dynamic light scattering (DLS) for more accurate size and weight measurements.

1.3.2 Dynamic Light Scattering

Dynamic light scattering is a light scattering technique that measures particle size based on their diffusion coefficient. Due to random Brownian motion of the particles in a liquid sample, scattered light intensity fluctuates with time.[35] Smaller particles diffuse faster than larger ones, which is measured by the time-dependence of the intensity fluctuations. A temporal autocorrelation applied to the time-dependent light scattering extracts the ensemble diffusion coefficient of the solution of particles, which can be converted to a particle size using the Stokes-Einstein equation. A main deficiency of DLS is its inability to provide quantitative measurements for a polydisperse distribution of particles.[36] DLS is highly sensitive to contamination and filtering the sample beforehand may also result in changing the particle distribution. DLS is limited to qualitative measurements and is unable to give quantitative measurements of particle counts and size distribution without being combined with other methods.[32]

1.3.3 Electron Microscopy

Electron microscopy allows for direct visualization of single particles and can be used to characterize size ranges between the nanometer and micrometer scale. It utilizes the fact that the wavelength of directed electron beam is several orders of magnitude lower than visible light to give an extremely high-resolution imaging potentially down to 0.1 nm.[37] Transmission electron microscopy (TEM) has been shown to be a viable orthogonal characterization technique due to the wide size ranges it can probe and can be automated for semi-quantitative subvisible particle measurement.[38] Although electron microscopy allows for resolving protein aggregates down to the nanometer scale, its

requirement for highly-trained operators and time consuming instrument alignment limits its use as a primary characterization method.

1.3.4 Resonant Mass Measurement

Resonant mass measurement (RMM) is a characterization method that uses a resonating cantilever and microfluidic channel to measure absolute size and size distribution of individual subvisible particles. The resonant frequency of the cantilever is mass-dependent, and is changed as particles flow through the microfluidic channel.[39] Precise frequency measurements thus allow for measuring the mass that was added or removed. When applied to subvisible protein aggregates, RMM uses microfluidic channels to push the sample through a sensor with an applied resonating frequency. RMM has potential to be an effective quantitative characterization method of subvisible particles and is capable of measuring size and distribution of polydisperse samples.[40]

1.3.5 Tunable Resistive Pulse Sensing

Tunable resistive pulse sensing (TRPS) measures size-dependent changes in electrical resistance caused by a particle passing through a nanopore. Tuning the pore size, voltage, and applied pressure allows for precise measurements of individual particles. It has been applied to subvisible protein aggregates and can quantitatively measure size and distribution over a wide size range.[41] Fundamentally, TRPS is an electrical-based method that has potential to be an effective orthogonal characterization tool along with other methods. RMM and TRPS both are precise single-particle measurement methods with no need for averaging.[42]

1.3.6 Microflow Imaging

Microflow imaging (MFI) characterizes subvisible particles by direct bright-field optical microscopy of a sample as it moves through a flow cell. Multiple frames are imaged successively and analyzed in real time to produce quantitative measurements of size, counts, and concentration.[43] Much of the imaging and analysis is automated, which allows for identifying different sample populations using image filtering. MFI has been used to effectively distinguish protein aggregates from other contaminants, although the spatial resolution is diffraction limited to about 1 μm.[44]

Table 1.1. Summary of characterization methods and their effective size range and applications

Method	Size Range	Application
SEC	1 nm - 100 nm	Size and count
DLS	1 nm - 1 µm	Size estimation and distribution
Electron Microscopy	5 nm - 10 µm	Size and morphology
RMM	50 nm - 5 µm	Size, distribution, count, mass, density, viscosity
TRPS	40 nm - 10 µm	Size, distribution, count, concentration, zeta-potential
MFI	1 µm - 50 µm	Size, distribution, count, concentration

1.4 Goal and Outline of the Thesis

The purpose of this thesis is to demonstrate interferometric scattering (IFS) microscopy's ability to characterize the size and surface structure of monoclonal antibody aggregates on a single-particle scale. We will examine two variants of IFS microscopy: (1) Multichannel imaging to correlate the size and surface structure of submicron protein

aggregates on a single-particle scale with correlative IFS and fluorescence microscopy. (2) hyperspectral interferometric scattering microscopy (h-IFS) microscopy to distinguish and quantify submicron protein aggregates and contaminants in biologics based on their scattering intensity spectra.

Specifically, the following questions will be addressed.

Correlative IFS and fluorescence microscopy questions:

- How can IFS and fluorescence microscopy be used in conjunction to correlate particle size and surface structure on a single particle scale?
- How does the surface structure of protein aggregates change as a function of aggregate size?

h-IFS microscopy questions:

- How can IFS be used to measure the optical scattering spectra of single protein aggregates?

The correlative imaging questions will be addressed in chapter 2. Starting from an overview of IFS microscopy, we address critical gaps in characterization methods of submicron protein aggregates. Following that, we will specifically review studies of Fc binding effects and protein aggregate structure. We then examine and discuss the results of imaging experiments using correlative IFS and fluorescence microscopy to correlate protein aggregate size and surface structure characteristics. Using Nile red and fluorescent anti-human IgG1 secondary antibodies as fluorescent labels, we found that surface Fc regions and hydrophobic groups were more concentrated on the surface of smaller protein aggregates (< 100 nm) compared to larger aggregates. In chapter 3, we discuss the utilization of h-IFS microscopy as a tool for characterizing optical properties of protein aggregates and nanoparticles. We present an overview of h-IFS microscopy

and the potential particle property information that can be gained. Then, we will demonstrate our imaging procedure and demonstrate examples of individual particle h-IFS spectra and briefly discuss the use of h-IFS for classifying nanoparticles of different composition/material in biopharmaceutical formulations. Chapter 4 summarizes the thesis and briefly discusses future work.

Chapter 2: Investigating Surface Structure of mAb Aggregates[1]

2.1 Overview

In this section, we will discuss gaps in protein aggregate characterization methods and the utility of IFS microscopy in filling those gaps. Then, we present and discuss the results of correlative IFS and fluorescence microscopy to characterize physical and chemical properties of mAb aggregates. Specifically, we will examine the following attributes of mAb aggregate surface structure as they relate to aggregate size by correlating IFS and fluorescence intensity: (1) surface Fc region presentation and (2) surface hydrophobic residues. Finally, we will discuss the potential of using IFS microscopy to characterize surface structure as well as possible relationships between mAb aggregate size, surface structure, and immunogenicity.

2.2 Interferometric Scattering Microscopy

Interferometric scattering microscopy is a label-free optical microscopy technique with enhanced resolution down to nanoscale particles and can be used to characterize submicron protein aggregates. A simple IFS setup is shown in Figure 2.1. Conventional optical microscopy methods are unable to resolve submicron sized protein aggregates. IFS uses wave interference to increase contrast between the sample and background and effectively increases the resolution limit to about 100 nm. When the sample is illuminated, the light scattered off the sample interferes with a reference wave and

[1] Note: Portions of the experimental methods section in this chapter were previously published by Wong et al. and are reproduced here with some modifications: Wong, N. A.; Uchida, N. V.; Dissanayake, T. U.; Patel, M.; Iqbal, M.; Woehl, T. J., Detection and Sizing of Submicron Particles in Biologics With Interferometric Scattering Microscopy. *Journal of pharmaceutical sciences* **2020,** *109* (1), 881-890.

reflects back to a detector in the microscope. Different interference patterns from the background and sample result in high-contrast images that allow detection and characterization of single aggregates. Rayleigh scattering describes the phenomenon of particles scattering electromagnetic radiation waves with wavelength much larger than the particle size. The scattered light intensity depends on radius raised to the sixth power; this relationship describes conventional optical microscopy methods with a lower resolution limit of about 500 nm. For example, the size difference between a 50 and 500 nm particles is 10x, but the scattering intensity difference would then be 1,000,000x. By interfering the particle scattering with a reference wave, IFS modifies the scaling relationship between scattered light intensity and particle radius to be cubic instead of to the sixth power, allowing for greater sensitivity to weakly scattering particles. In Figure 2.1, results are shown from a previous study where we demonstrated the ability of IFS to detect and measure the size of submicron protein aggregates.[45]

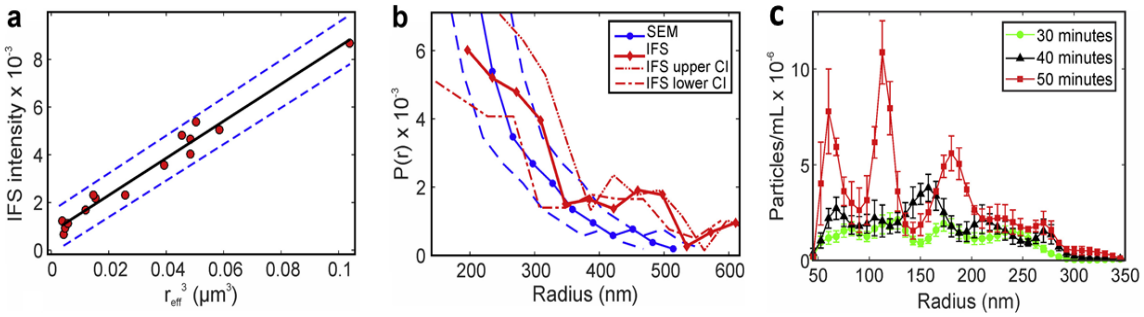

Figure 2.5. (a) Calibration curve derived from SEM and IFS data after excluding shape anisotropic and nonprotein particles. The black line is the least squares fit, whereas the dashed blue lines represent the 95% confidence intervals resulting from the standard fitting error. (b) PSD determined from direct particle sizing with SEM (blue circles) and calibration of the IFS intensity distribution using the calibration curve in (a) (red diamonds). (c) Nanoparticle tracking analysis measurements of the particle size distribution of protein aggregates formed at various stir times. Error bars represent the standard deviation of the distribution from at least 3 trial replicates in a single sample. Figure and caption reproduced from Wong[45].

The main advantages of IFS are its simplicity of sample preparation, equipment operation, and data analysis.[45,46,47] Now in this thesis, we will expand its application to surface structure characterization.

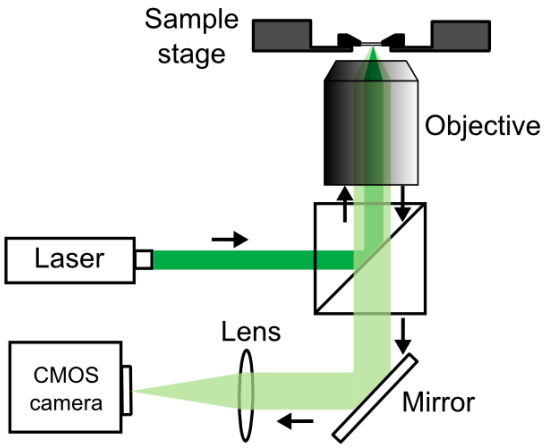

Figure 2.6. Example schematic of interferometric scattering microscopy setup using a common path interferometer. Reproduced from Hsieh[48].

2.3 Gaps in Protein Aggregate Characterization Methods

Recent studies have shown that factors other than protein aggregate size and count affect their immunogenicity. In chapter 1, we highlighted protein aggregate surface attributes as a potential factor. While the FDA currently only regulates aggregates based on their size and count, *i.e.* their physical properties, new analytical techniques are required to characterize biophysical and biochemical properties given that these properties will affect how the aggregates interact with the immune system. Most current analytical techniques, such as SEC and DLS described previously, inherently use averaging in ensemble measurements and only probe the particle size or molecular weight; furthermore they are unable to characterize aggregate morphology.[16,38] Fc

binding site surface presentation of aggregates may be an important characteristic of mAb aggregates for understanding their immunogenicity. Tada et al. have shown that differences in aggregate Fc structure cause different levels of Fc receptor activation, which suggests Fc structure plays a role in causing immunogenicity.[31,49] Antibody Fc binding is key to activating various immune responses, such as antibody-dependent cellular cytotoxicity and in maintaining humoral tolerance. Aggregate Fc receptor activation can trigger the release of inflammatory cytokines. Breaking of B-cell tolerance has been suggested as another possible immunogenicity mechanism.[50] In *in vitro* immunoassay experiments, Joubert et al. showed that T-cell immune response levels are affected by protein structure in the aggregates, such as their degree of unfolding, and immune response activation was likely mediated by specific binding of Fc receptors to Fc regions of mAb aggregates.[51] Hydrophobic interactions are known to play a large role in protein aggregate formation and studies have shown the hydrophobic sequences in therapeutic mAb aggregation-prone regions are located in T-cell epitopes.[52] These recent studies suggest that hydrophobic residues and Fc regions on the protein aggregate surface are important factors in immunogenicity, and thus are the primary characteristics examined in this chapter.

2.4 Experimental Methods

2.2.1 Protein Aggregates

NISTmAb (IgG1κ, MW ≈ 150,000, Standard reference material #8671) (Figure 2.3), was obtained at a concentration of 100 mg/mL in 25 mM l-Histidine buffer (12.5 mM L-His, 12.5 mM L-His HCl, pH = 6).[53] The protein was diluted to 1 mg/mL with the

same buffer and filtered through a 200 nm syringe filter. The diluted protein was aliquoted into sterile particle-free 3 mL glass vials, each containing an 8 × 2 mm Teflon stir bar. The vials were stirred for 3 hours at 1000 rpm. Stir bars were removed from the vials, and the samples were characterized undiluted. Samples were stored in the refrigerator prior to characterization.

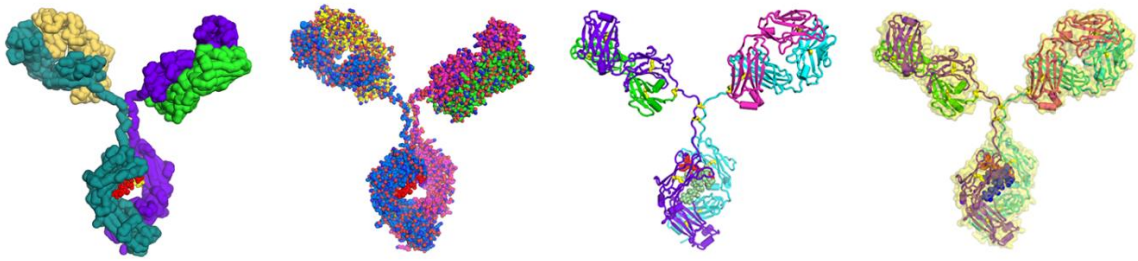

Figure 2.7. Structure of NISTmAb reference material 8671. Reproduced from NIST[54].

2.2.2 Interferometric Scattering Microscopy and Sensors

Layered sensor chips were prepared for the sample substrate starting with a 100 mm silicon wafer. A 60 nm thick silicon oxide (SiO_2) layer on top of the wafer was fabricated by first depositing a 110 nm thermal SiO_2 layer and then wet etching with hydrofluoric acid.

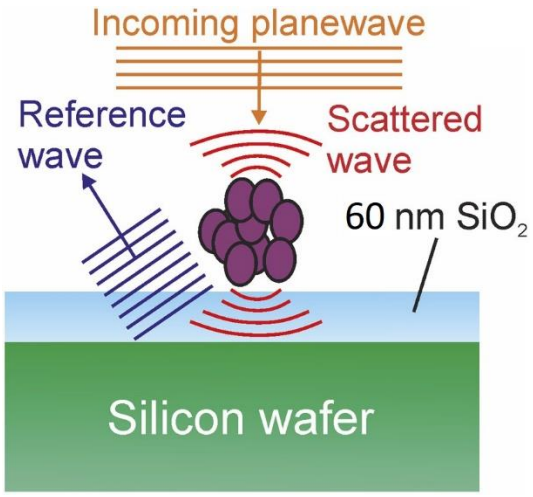

Figure 2.8. Schematic cartoon of multilayered IFS sensor and optical scattering and interference. An incoming planewave scatters off a protein aggregate (purple). The planewave also reflects off the silicon-silicon oxide interface and produces a reference wave, which interferes with the scattered wave. The interference pattern is observed on a CMOS camera on a modified optical microscope. Figure and caption reproduced from Wong[45].

The IFS sensors were prepared by cutting the surface oxidized silicon wafer into 1 × 1 inch pieces and cleaning with Alconox and water, followed by sonication in acetone, methanol, and DI water for 10 min each. The sensor chips were dried with filtered air and plasma cleaned for 5 min in an air plasma (Harrick Plasma, PDC-32G) to remove residual solvent and surfactant from the sensor surface. Ten microliters of liquid protein aggregate sample was pipetted onto each sensor surface, dried at room temperature, and rinsed with DI water. Protein aggregates were imaged dry because the large refractive index difference between air and SiO2 increases the sensitivity of IFS.[55] While imaging the protein aggregates dry may change their size/shape, recent measurements of protein aggregate density indicate that density tends exponentially toward the theoretical density of a protein ($\rho \approx 1.3 g/cm^3$) for submicron protein

aggregates. This suggests that submicron protein aggregates contain little porosity and that their size will not be significantly affected by drying.

IFS experiments were performed on a modified inverted optical microscope (Zeiss Axio Observer) operated in reflection mode. The microscope was equipped with a multi-wavelength LED light source for the Fc binding experiments and with a xenon arc lamp for the hydrophobic residue experiments. IFS images were acquired with a 20x dry objective lens with a numerical aperture of NA = 0.45 and projected onto a monochrome 1900 × 1200 pixel CMOS camera with an exposure time of 1 ms. The same LED intensity and camera exposure time were used for each sample to facilitate automated image analysis. A 1 mm diameter pinhole was inserted into the back focal plane of the objective lens to decrease the NA of the objective lens. This modification increases the IFS image contrast by illuminating the sample at low angles of incidence, which directs light scattered from the particles into the objective lens as opposed to scattering to wide angles, decreasing the background of the IFS image.[56] A single sample area was imaged over 35 time points each at 20 stage focal heights (0.22 μm interval between focal heights). The z-slice range is manually centered on the most in-focus stage height. The resolving power of this IFS optical system is expected to be about 100 nm in diameter for weakly scattering particles, as confirmed in previous experiments we have conducted.[45]

2.2.3 Fluorescence Labeling and Microscopy

Protein aggregate Fc regions were labeled with secondary antibodies conjugated with AF488 fluorescent dye (excitation maximum 490 nm, emission maximum 525 nm) obtained from ThermoFisher (mouse anti-human IgG1 Fc secondary antibody, Alexa

Fluor 488). The labeling procedure was adapted from direct immunolabeling procedures modified to use the Fc-binding secondary antibody as a primary antibody. The original label concentration was 1 mg/ml in PBS buffer (pH = 7.4) and was diluted to 1 µg/ml in the same buffer. As a control, fluorescein-conjugated bovine serum albumin (BSA) solution was prepared at 1 µg/ml in the same PBS buffer from its original lyophilized form (ThermoFisher). A BSA solution was used during the labeling procedure as a blocking agent. One vial each of 1% and 0.1% BSA solution was prepared in PBS buffer from the original lyophilized powder.

For the surface-exposed hydrophobic residue experiments, Nile red dye (MW ≈ 319 g/mol) was used. Nile red fluoresces strongly when bound to hydrophobic residues (excitation maximum 554 nm, emission maximum 638 nm), and is weakly fluorescent in water. Three concentrations of Nile red were prepared for labeling in separate vials from the original lyophilized powder: 1 µM, 15 µM, and 67 µM.

In the Fc domain presentation experiment, two IFS sensors were prepared with dried protein aggregates on the surface as described in section 2.2.2. A thin layer of 1% BSA blocking agent was then deposited on the sensor chip surface and left to incubate at room temperature for 1 hour before washing with deionized water. The anti-human IgG1 Fc secondary antibody solution and the BSA-fluorescein control solution were both mixed with 0.1% BSA blocking agent and incubated at room temperature for 3 hours. After the incubation period, 100 µL of each mixture was deposited on separate sensor chips and incubated at room temperature for 1 hour. Finally, both sensor chips were washed with PBS buffer and deionized water. A schematic of the Fc domain binding is shown in Figure 2.5.

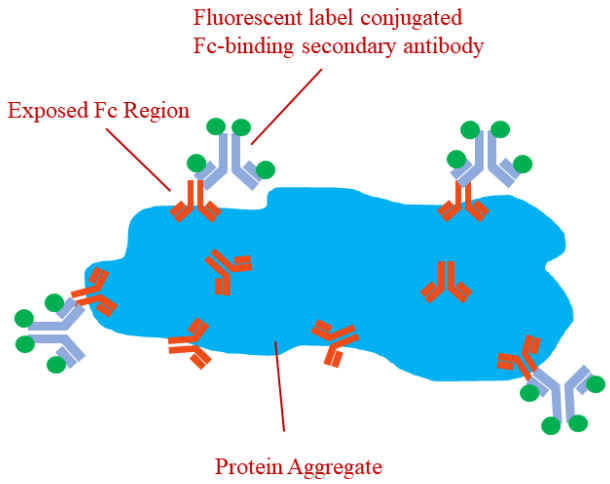

Figure 2.9. Schematic of Fc region fluorescence labeling. A protein aggregate labeled with anti-human IgG1 Fc secondary antibody conjugated with AF488 fluorophores.

In the last experiment, surface hydrophobic residues were labeled by mixing the protein aggregate sample with the 1 µM, 15 µM, and 67 µM Nile red solutions at a 1:1 ratio in 3 different vials and left to incubate for 1 hour at room temperature. Then, 10 µL of each mixture was deposited on 3 different prepared IFS sensors.

The same microscope used for IFS imaging was converted to fluorescence mode by swapping filters sets. Using the xenon lamp, a green excitation filter set was used for IFS and a red emission filter set was added for fluorescence imaging. After an image was taken in IFS mode, the microscope was converted to fluorescence mode and the same sample area was imaged again.

2.2.4 Image Processing

Figure 2.6 shows the method used to process each IFS image. All image processing and analysis was performed with in-house MATLAB routines. IFS images were acquired and processed in 16-bit format to give 65,536 possible gray values for intensity quantification of protein aggregate size. The averaged IFS sample image $\langle I_S \rangle$ and IFS background image $\langle I_B \rangle$ were pseudo-flat fielded by first subjecting them to a 2D median filter with a large filter size of 150 × 150 pixels. This filtered image is a pseudo-background, which was subsequently subtracted from the original IFS images to give constant background intensity, $\langle I_{S,ff} \rangle$ and $\langle I_{B,ff} \rangle$. The flat-fielded IFS sample image was then subtracted from the background image to remove dust particles and optic imperfections near the focal plane. The final processed IFS images, $^{35} = \langle I_{B,ff} \rangle - \langle I_{S,ff} \rangle$, showed aggregates as bright scattering centers on a dark background, which facilitated subsequent image segmentation.

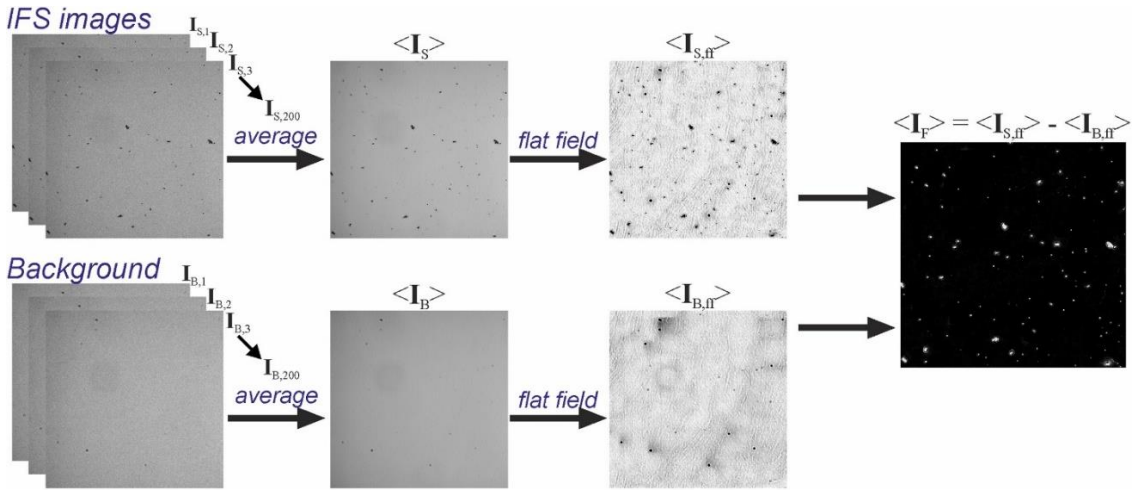

Figure 2.10. Image processing routine for flat fielding and removal of background artifacts from IFS images. Brackets denote the average of 200 images. The final processed image, I_F, was processed with image segmentation. Figure reproduced from Wong[45].

While protein aggregates weakly scatter light, background subtraction and flat fielding removed essentially all background noise and enabled efficient and accurate binarization of IFS images. Image analysis quantified the maximum scattering intensity of each particle on a 16-bit scale. A discriminating function was included in the image analysis algorithm that distinguished between point scatterers, which have intensities that are quantitatively proportional to their mass, and larger shape anisotropic particles whose scattering intensity is ill-defined by theory. This function was set to excluded large (>1 μm) asymmetric particles from the image analysis.

To correct for slightly different focal heights of protein aggregates with different sizes, each sample region was imaged with IFS at 20 different focal heights with a 0.22 μm interval between slices (Figure 2.7). Small errors in the focal plane result in inaccuracies in measuring the relative size of each particle based on maximum IFS intensity. Each particle's x-y position was tracked and recorded from the image centered in the z-slice range; the maximum intensity value was then recorded as the particle IFS intensity.

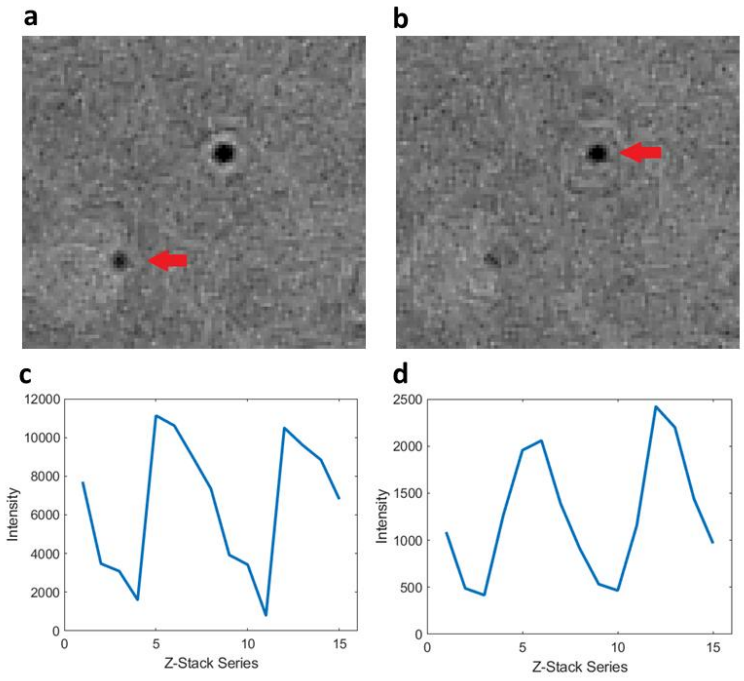

Figure 2.11. IFS images taken at different focal heights, (a) z = 5 (b) z = 12, with red arrows marking the in-focus particle. Plots of the particle's intensity vs. z-slice, (c) corresponding to image (a), and (d) corresponding to image (b). Intensity is highest at the in-focus slice.

Following image segmentation, the total number of particles per image and maximum particle scattering intensities were recorded in a data structure. Figure 2.8 shows an example of the IFS and fluorescence image for Nile red labeled protein aggregates. The fluorescence images underwent similar processing and analysis in MATLAB as the IFS images. Image analysis data collected from the IFS and fluorescence images from each area of a sample were combined into a single data structure to determine the correlation between relative particle size (IFS intensity) and fluorescence.

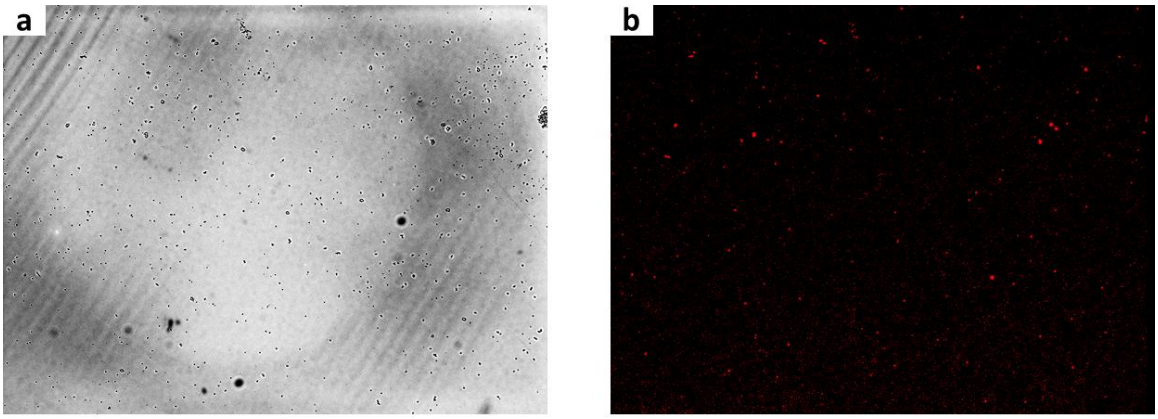

Figure 2.12. Raw images of a Nile red-labeled protein aggregate sample taken in (a) IFS mode and (b) fluorescence mode. The IFS image was taken over 35 time points each at 20 focal heights, totaling 700 images.

2.2.5 Bulk Fluorescence Measurements

To support the protein aggregate size dependence of the Nile red fluorescence imaging results, ensemble fluorescence measurements were performed on filtered protein aggregate samples bound with Nile red. Three protein aggregate samples were prepared in separate vials and each was filtered with a different syringe filter pore size: 0.22 μm, 0.45 μm, and 0.8 μm. Each filtered sample was mixed in a 1:1 ratio with 67 μM Nile red and their bulk fluorescence spectra was measured at an excitation wavelength of 554 nm in a multi-mode plate reader. The three filtered samples were deposited in separate wells of a 64-well transparent microplate, along with an unfiltered protein aggregate sample and a deionized water blank sample. Additionally, the absorbance of each sample was measured to account for differences in sample concentration by using the Beer-Lambert relationship of concentration of absorbance.[57]

2.5 Results and Discussion

2.3.1 Surface Fc Domain Imaging

Figures 2.9 and 2.10 shows the IFS intensity (I_{IFS}) and fluorescence intensity (I_{FL}) of single protein aggregates labeled with 1 µg/ml of the secondary antibody and BSA control.

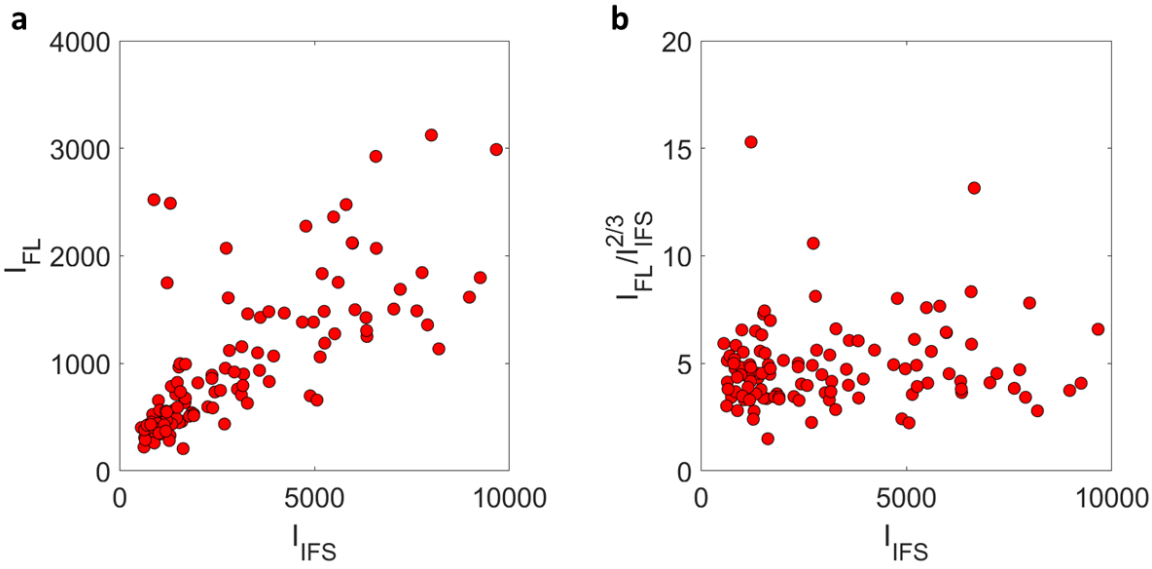

Figure 2.13. (a) I_{FL} vs. I_{IFS} of protein aggregates labeled with 1 µg/ml of anti-human IgG1 Fc-AF488 conjugate. (b) I_{FL} normalized to protein aggregate surface area as calculated by $I_{IFS}^{2/3}$.

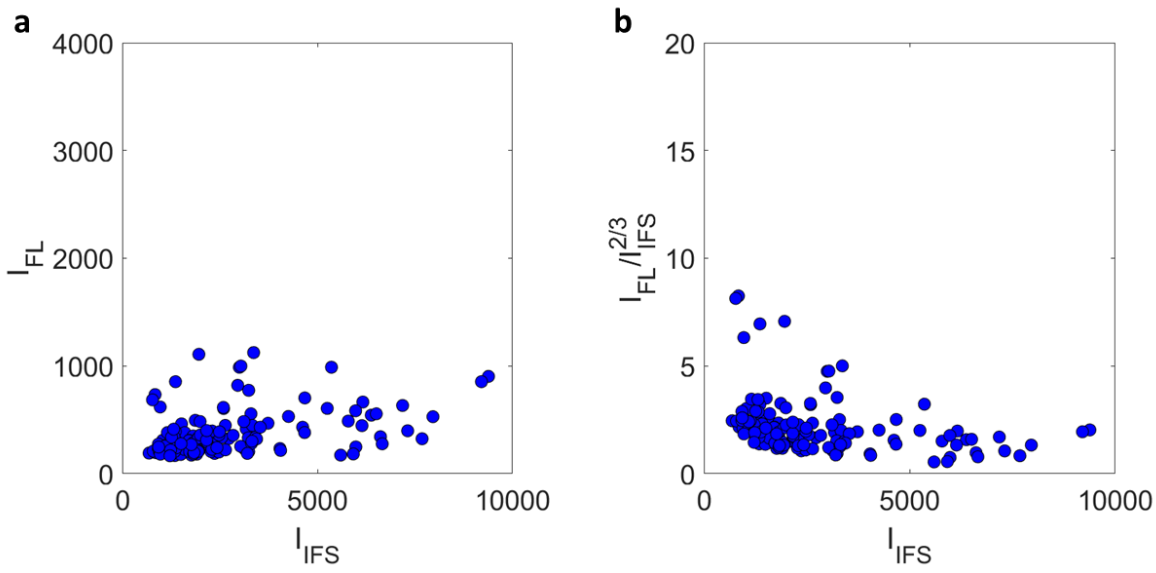

Figure 2.14. (a) I_{FL} vs. I_{IFS} of protein aggregates labeled with 1 µg/ml of BSA-fluorescein as a control. (b) I_{FL} normalized to protein aggregate surface area as calculated by $I_{IFS}^{2/3}$.

I_{FL} is directly proportional to the number of secondary antibodies bound to a protein aggregate, and thus to the number of Fc regions exposed on the protein aggregate surface. To determine the surface concentration of Fc regions, the fluorescence intensity should be normalized to the surface area of the aggregate. I_{IFS} is directly proportional to the volume of the particle, thus the IFS intensity raised to the 2/3 power ($I_{IFS}^{2/3}$) is proportional to the particle surface area. In the sample labeled with 1 µg/ml of the secondary antibody I_{FL} increases with I_{IFS}, which means the number of surface Fc regions increases with particle volume and size. If the number of surface Fc regions was proportional to surface area, *i.e.* if Fc surface concentration is not dependent on aggregate size, then the fluorescence intensity normalized to particle surface area ($I_{FL}/ I_{IFS}^{2/3}$) would be expected to show a flat trend with respect to I_{IFS}. Indeed, this is what is observed in Figure 2.9.

BSA-fluorescein was used as a control label and a blocking agent because it non-specifically binds to the protein aggregate surface.[58] The BSA-fluorescein labeled control sample informs us how effective the labeling and rinsing procedure was at eliminating non-specific binding to charged groups. Since the secondary antibody label and control BSA-fluorescein have slightly different degrees of labeling (anti-IgG1 Fc AF488: 6, BSA-fluorescein: 5) and the fluorescent labels have different quantum yields, so the measured I_{FL} values for the control and labeled sample cannot be directly compared. However, the measured I_{FL} values seen in the control sample (Figure 2.10 (a)) were generally low compared to those seen in Figure 2.9 (a) and were not a function of the protein aggregate size. The flat relationship between I_{FL} and I_{IFS} in Figure 2.10 (b) shows that BSA binding is not specific or particle size-dependent and indicates the I_{FL}-I_{IFS} correlations in Figure 2.9 are a result of specific Fc region binding.

It is possible that the size independent surface concentration of Fc labels shown in Figure 2.9 (b) was due to an insufficient amount of Fc-specific fluorescent label, so we prepared another sample labeled with 10 μg/ml (10x more concentrated compared to Figure 2.9) of the secondary antibody (Figure 2.11) and with BSA-fluorescein (Figure 2.12).

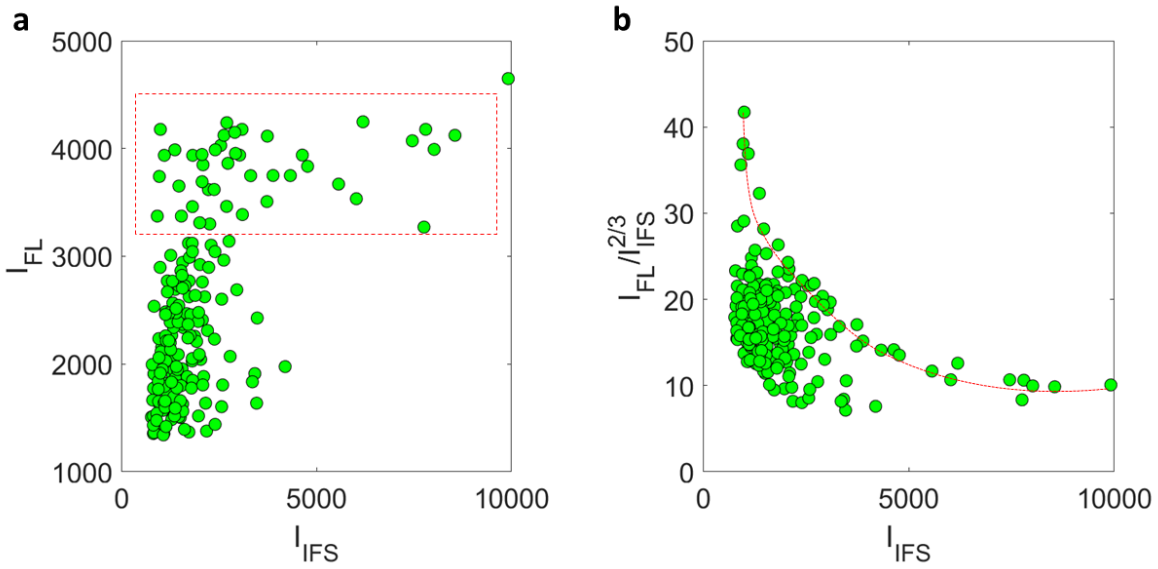

Figure 2.15. (a) I_{FL} vs. I_{IFS} of single protein aggregates labeled with 10 µg/ml of anti-human IgG1 Fc-AF488 conjugate. (b) I_{FL} normalized to protein aggregate surface area as calculated by $I_{IFS}^{2/3}$. Red dotted boxes in (a) and lines in (b) mark a distinct population of particles with binding behavior not observed in the control sample.

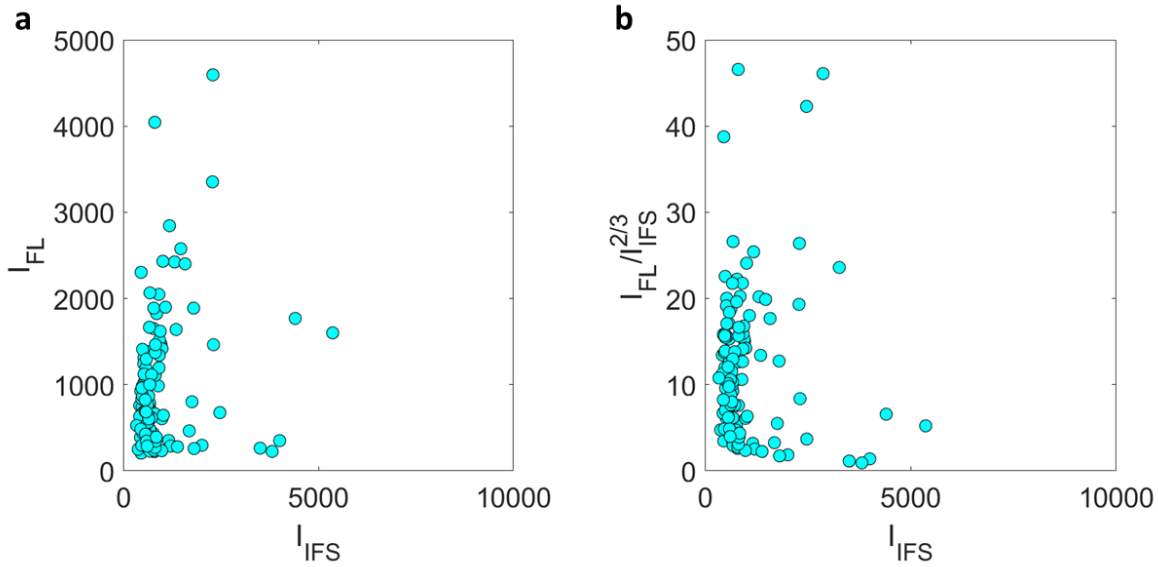

Figure 2.16. (a) I_{FL} vs. I_{IFS} of single protein aggregates labeled with 10 µg/ml of BSA-fluorescein as a control. (b) I_{FL} normalized to protein aggregate surface area as calculated by $I_{IFS}^{2/3}$.

Overall, the measured I_{FL} values were higher compared to the 1 µg/ml samples, suggesting that the surface Fc regions were not completely bound. The minimum I_{FL}

value seen in Figure 2.11 (a) was greater than 1000, whereas about 75% of the particles in Figure 2.9 (a) showed an I_{FL} value less than 1000. In Figure 2.11 (a), the IFS-fluorescence intensity correlations showed a qualitatively different trend compared to the 1 µg/ml label concentration sample. For I_{IFS} values ranging from 1000-2000 the fluorescence intensity varied widely from 1200 – 4000 (Figure 2.11 (a)). Based on the BSA control sample in Figure 2.10 (a), this grouping of particles had significant non-specific binding of the antibody label. Interestingly, there was a distinct grouping of particles highlighted by the red dotted box in Figure 2.11 (a), which showed high fluorescence intensity that was size invariant. The red line highlights these particles in the surface concentration plot in Figure 2.11 (b), which showed an exponential decay of surface concentration with increasing I_{IFS}. In this sample, smaller protein aggregates showed higher label binding, and thus higher surface concentrations of Fc domains, compared to larger ones. This trend was not seen in the control sample in Figure 2.12, but there was a similar large spread of I_{FL} values over a narrow range of I_{IFS}. Since it was observed in both the experimental and control samples, the large I_{FL} spread for particles of similar size was likely a result of increased nonspecific binding due to the higher label concentration used.

One observation common to both label concentrations was that I_{FL} was generally more scattered at larger I_{IFS} values, making it difficult to separate surface structure trends from noise. We hypothesize that the larger protein aggregates of $I_{IFS} > 5000$ were more porous and non-spherical than smaller aggregates. The increased porosity caused more noisy data for two reasons: (1) Higher porosity changed the refractive index of larger protein aggregates and affected IFS scattering intensity differently than less porous

particles and (2) higher porosity also generally invalidates the assumption of spherical protein aggregates. More porous particles might have higher or lower effective surface area, depending on whether the pore size permitted binding of the label to Fc regions.

The mechanism for Fc domain enrichment on the surface of smaller protein aggregates could be explained by the aggregate formation mechanism. Sediq et al. found that formation of protein aggregates during stirring is likely preceded by abrasion of the protein monomer as it is adsorbed to the solid container surface adjacent to the magnetic stirrer.[59] After initial adsorption to the surface, abrasion caused by the stirrer leads to partial unfolding of the monomer. Then, the structurally perturbed monomer can either desorb from the solid surface or initiate aggregation on the surface itself.[59] The orientation of the adsorbed IgG antibody might then play a role in favoring higher surface Fc presentation in smaller protein aggregates of the submicron range. Wang et al. found that IgG adsorption to hydrophilic surfaces was primarily in the flat-on orientation, meaning both the Fc and Fab regions are laid flat on the solid surface.[60] Whereas on hydrophobic surfaces, Wiseman et al. found that IgG antibodies adsorption orientation was “flat-on” until reaching half-monolayer coverage after which vertical orientation of IgG, either with the Fc region pointed towards the solid surface (Fab-up) or pointing toward the bulk solution (Fab-down), becomes preferred.[61] It is possible that the stirring conditions we used favored a certain adsorption orientation, leading to protein aggregates with higher surface presentation of Fc regions. Later stages of stirring induced protein aggregation proceed by aggregate-aggregate attachment, which would randomize the display of Fc regions on the aggregate surface due to the non-specific nature of the aggregate attachments between small and large aggregates. These results provide

evidence that smaller nanometer-sized protein aggregates may have greater ability to activate Fc receptors and potentially generate immunogenic reactions.

2.3.2 IFS and Fluorescence Microscopy of Surface Hydrophobic Groups

In Figure 2.13, we show the IFS-fluorescence intensity correlations of protein aggregates samples labeled with three concentrations of Nile red: 1 μM, 15 μM, and 67 μM. There was not a trend observed between the measured fluorescence intensity and the IFS intensity (Figure 2.13 (a),(c),(e)). Once normalized to the particle surface area, the fluorescence intensity showed a power law decay with the interferometric scattering intensity (Figure 2.13 (b),(d), (f)). The decay and normalized values of the fluorescence intensity did not vary significantly with label concentration. These data demonstrate that the presentation of hydrophobic groups was higher on smaller protein aggregates relative to surface area and decayed as particle size increased. This observed trend is similar to the one seen with Fc region presentation. Another common trend is the increased scattering of I_{FL} values at higher I_{IFS} values. Again, we hypothesize that larger aggregates having higher porosity is the cause of increased deviations.

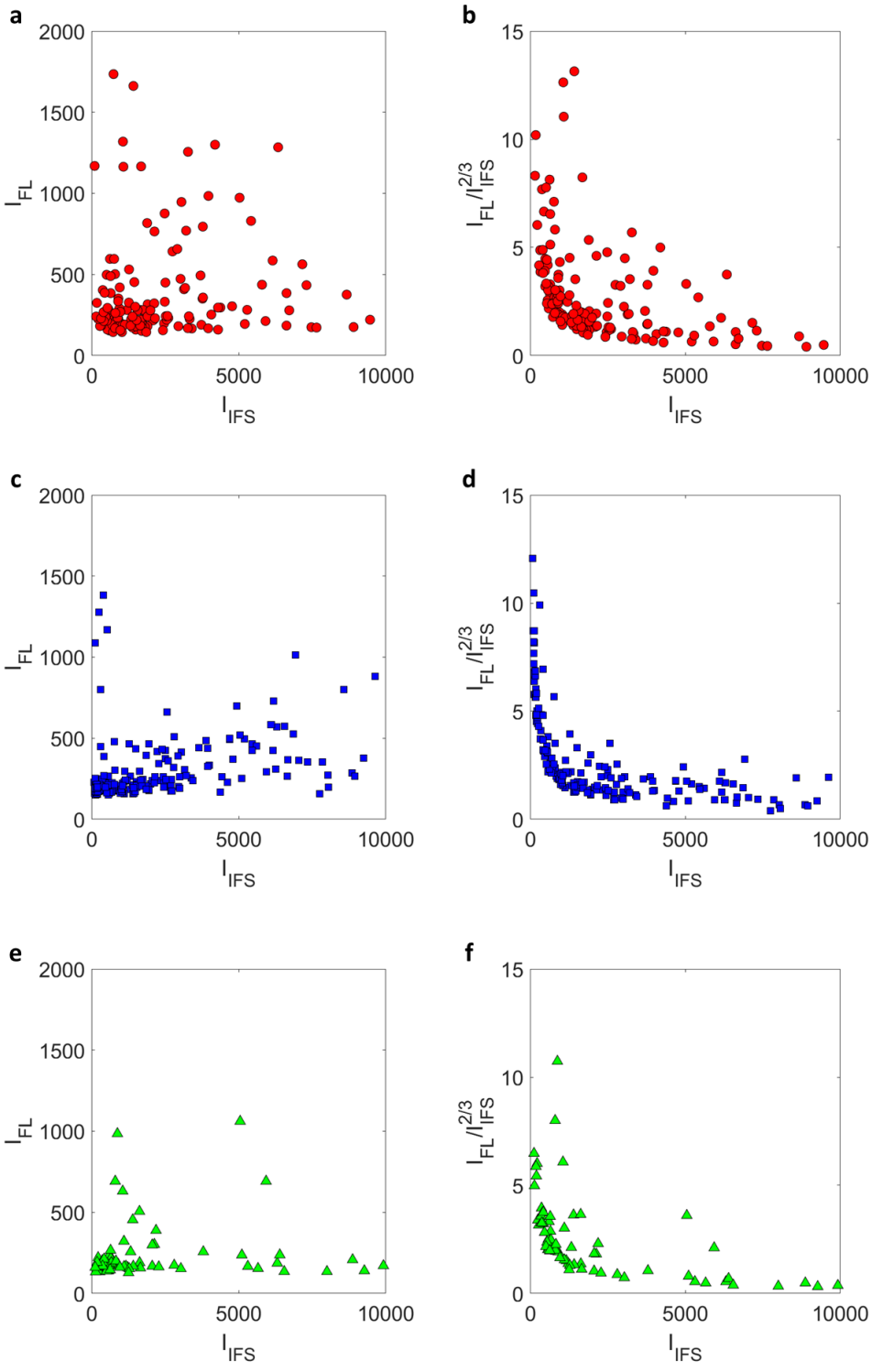

Figure 2.17. I_{FL} vs. I_{IFS} of protein aggregates labeled with Nile red, and I_{FL} normalized to protein aggregate surface area as calculated by $I_{IFS}^{2/3}$. Nile red concentration = (a) (b) 1 µM, (c) (d) 15 µM, (e) (f) 67 µM.

To confirm the results measured by our IFS-fluorescence microscopy method, we measured bulk fluorescence and absorbance of protein aggregate samples labeled with 67 μM Nile red using fluorescence spectrometry and filtered through 0.22, 0.45, and 0.8 μm syringe filters. Each filtered sample excluded protein aggregates larger than the filter pore size. The absorbance of each sample was measured at 280 nm to determine the relative protein concentration using the unfiltered protein aggregate sample's absorbance as a reference value, since the extinction coefficient of aggregated protein is not known. Then, the fluorescence spectra of the filtered sample was normalized by the relative concentration to enable direct comparison of each sample (Figure 2.14). The 0.22 μm filtered sample showed the highest peak fluorescence, followed by the 0.8 μm and then the 0.45 μm filtered sample, indicating that the smallest protein aggregates exhibited the highest Nile red binding. However, the 0.8 μm filtered sample having higher fluorescence than the 0.45 μm filtered sample did not agree with the IFS-fluorescence microscopy results. These results indicate that smaller sized protein aggregates (~100 nm) may have higher potential for hydrophobic interactions with cells and other proteins in the blood stream.

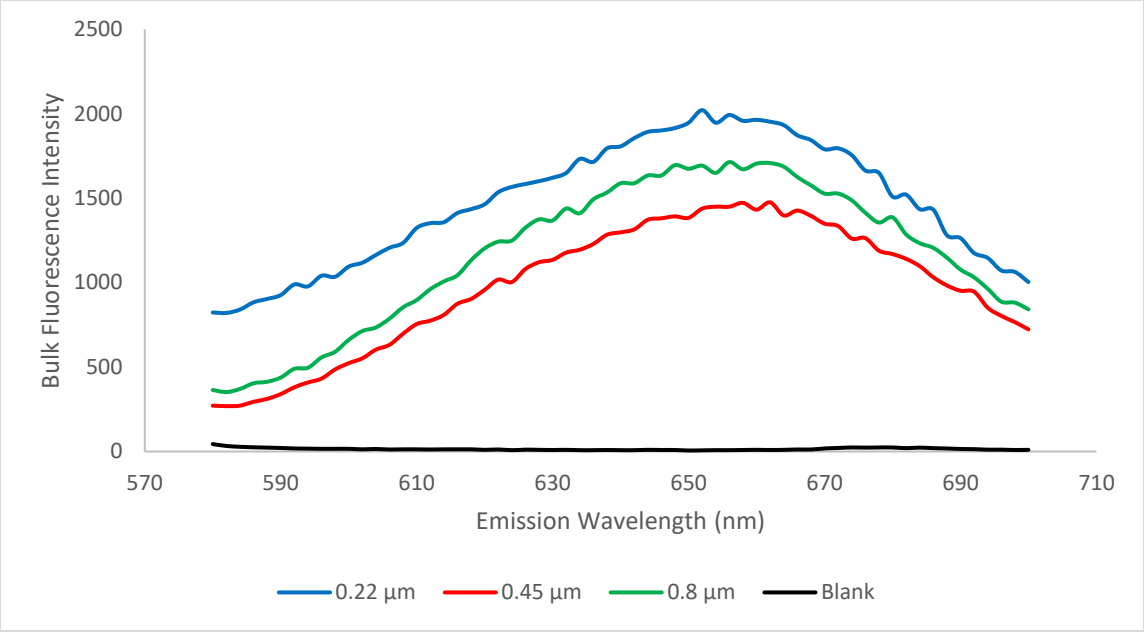

Figure 2.18. Bulk fluorescence spectra of protein aggregate samples filtered with different pore sizes and normalized to relative concentration. Unfiltered and blank samples were also included, all samples were measured at an excitation wavelength 554 nm.

Figure 2.19 shows a diagram of an IgG antibody, buried hydrophobic residues prone to aggregation are highlighted in red.

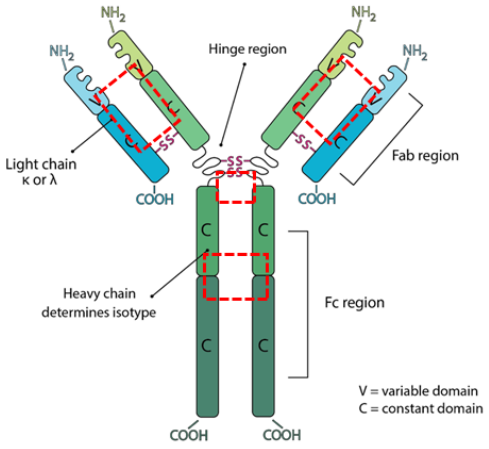

Figure 2.19 Structure of an IgG antibody with red boxes highlighting aggregation-prone buried hydrophobic residues. Original figure reproduced from Bxcell[5].

2.6 Conclusions

To summarize, our results provided evidence that smaller protein aggregates of sizes in the range of < 500 nm present higher surface concentrations of Fc domains and hydrophobic groups. The latter was supported by ensemble fluorescence measurements. However, without a size-calibration curve, determining the precise size from measured I_{IFS} values was not possible. Inherent noisiness in our data requires better methods of eliminating nonspecific binding either during the labeling procedure, which will be discussed in Chapter 4.

Chapter 3: Hyperspectral Interferometric Scattering Microscopy as a Biologics Characterization Method

3.1 Overview

In Chapter 2, we discussed the need for more advanced and simple-to-use characterization methods of protein aggregates in biopharmaceutical products. In addition to protein aggregates, trace amounts of non-protein particulate contamination are present in biologics, such as silicone oil droplets and metal particles resulting from processing and packaging. These contaminants serve as nucleation sites for protein aggregation and pose additional health risks.[62,63] Furthermore, current analytical methods such as DLS and MFI cannot distinguish the composition of particles, only their size.[43,64] Thus, additional analytical methods are needed to characterize the composition of protein aggregates and non-protein contaminants found in biologics.

In this section we discuss the development of hyperspectral IFS (h-IFS) as a potential characterization method to solve this problem. We start with a discussion of the

importance of characterization and quantification of submicron non-protein contaminants in biologics. The next section covers h-IFS and what distinguishes it from conventional IFS microscopy, as well as its potential application to characterizing submicron protein aggregates and non-protein contaminants. Finally, we present and discuss the results of experiments using our previously discussed IFS setup modified with a multi-wavelength LED for h-IFS.

3.2 Contaminants in Biologics and Implications for Protein Aggregation

Vials and pre-filled syringes are the most common storage and delivery methods used for parenteral drugs in the biopharmaceutical market. Both methods require lubrication to function during delivery and manufacturing. Silicone oil is used for its ideal physiochemical properties, such as low surface tension, low immunogenicity, and hydrophobicity.[65] However, silicone oil can leach into the bulk drug solution and form emulsion droplets due to errors in the coating process as well as mishandling of the vials or syringes. The silicone oil droplet interface is hydrophobic which leads to protein adsorption and aggregation.[66] Over the storage lifetime of a therapeutic protein, the presence of silicone oil droplets can lead to increased aggregation and higher immunogenic risk.[67]

Contaminants leaching into the drug solution also occurs during contact with solid plastic, metal, and glass surfaces. Stainless steel surfaces in particular are known to leach iron, nickel, and chromium.[68] Chronic exposure to trace metal contaminants through biologics increases the risk of acute toxicity and longer-term health problems. Additionally, metal contaminants can cause faster protein degradation and lower the shelf

life of biologics. In some cases, metal contaminant-induced degradation leads to increased protein aggregation, which has significant consequences for immunogenicity. For example, tungsten oxide contamination introduced during manufacture of pre-filled syringes has been shown to cause protein oxidation and aggregation.[69]

3.3 Hyperspectral Interferometric Scattering Microscopy Theory

The relationship between particle size and IFS scattering intensity was previously discussed in chapter 2. The basis of h-IFS is the relationship between refractive index, incident light wavelength, and IFS scattering intensity. The refractive index, dielectric constant, and polarizability of a material are all related. They can be used to identify and differentiate particle types based on their optical scattering spectra. Protein aggregates and non-protein contaminants have different refractive indices that will lead to unique scattering intensity change with illumination wavelength, due primarily to changes in constructive and destructive interference.[70,71]

3.4 Experimental Methods

3.4.1 Protein Aggregates and IFS Sensors

Protein aggregate samples were prepared on IFS sensors with 100 nm thick SiO_2 layers. Both the protein aggregate samples and the IFS sensor were prepared with the same procedure described in chapter 2. A 100 nm SiO_2 layer was chosen for maximum sensitivity based on simulations using the Fresnel equations to calculate transmittance of protein aggregates on an air-SiO_2 interface.

3.4.2 h-IFS Imaging

The inverted microscope used in Chapter 2 was modified for h-IFS imaging. The instrument was equipped with a multi-wavelength LED with 7 wavelengths of incident light (385, 430, 475, 511, 555, 590, and 630 nm). For a given sample region and imaging LED wavelength, 25 images were recorded at each of 15 focal heights centered about the approximate focal plane as determined by manual observation. For each focal height the 25 images were averaged together to remove sample noise, followed by a background subtraction as described in Chapter 2. The IFS intensity of each particle was measured at the corrected focal height for each LED wavelength using the focal height correction procedure described in chapter 2. The scattering intensity of each particle at each wavelength was extracted using MATLAB and saved in a data structure.

3.5 h-IFS Experiments

We demonstrated our h-IFS microscope setup on NISTmAb protein aggregates prepared by methods described in Chapter 2. The IFS scattering intensity of each particle was measured and at each of the 7 wavelengths to prepared single particle scattering spectra. Figure 3.1 shows several h-IFS single particle spectra for protein aggregates of various sizes. The 4 spectra with the lowest I_{IFS} values ($I_{IFS} < 6{,}000$) showed a peak wavelength between 555 nm and 630 nm and represented the most common protein aggregate type seen in this sample, which were < 500 nm protein aggregates. The other 3 particles had different h-IFS spectra in terms of both the scattering intensity as well as the peak wavelength.

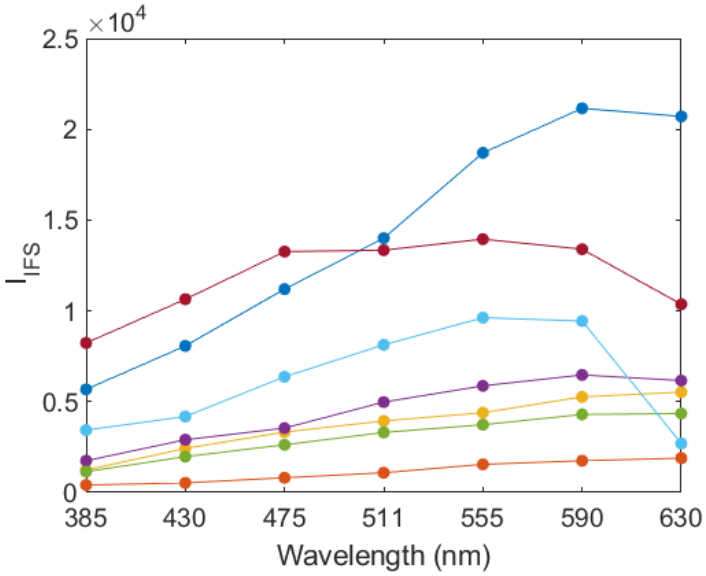

Figure 3.20. IFS scattering intensity spectrum of 7 particles in a protein aggregate sample measured from 7 wavelengths between 385 nm and 630 nm.

Figure 3.2 shows the maximum measured I_{IFS} value and the wavelength it was measured at for ~500 protein aggregates from a single sample area. Most particles with peak I_{IFS} values < 10,000 had peak wavelengths between 555 - 630 nm. Other particles with higher I_{IFS} values might either be larger non-spherical protein aggregates, which had significant porosity and thus different refractive index, or other non-protein contaminants. Using our sample and IFS sensor preparation method, we expect adventitious particle numbers to be around 1% of the number of protein aggregate particles.[45]

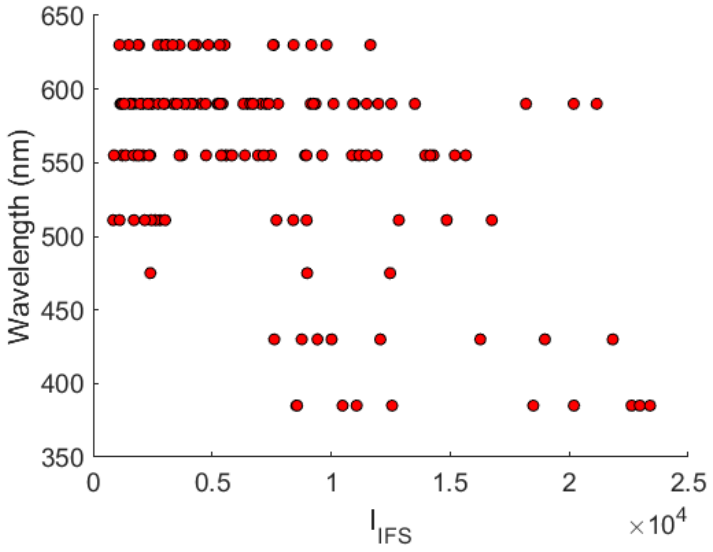

Figure 3.21. Peak I_{IFS} values and the wavelength of incident light they were measured at for single particles in a protein aggregate sample.

More experiments should be performed in order to fully develop a particle classification method based on h-IFS. For instance, previous work by Daaboul et al. developed a model to calculate the IFS intensity based on the refractive index and size of nanoparticles that could be employed here to classify nanoparticle and protein aggregate optical properties.[72]

3.6 Conclusions

The presence of non-protein contaminants in biologics has important implications in immunogenicity. In addition, the increasing importance of additional orthogonal characterization methods highlights the need to differentiate particle types in biologics. These results are a first demonstration of h-IFS to measure the scattering spectra of single protein aggregates. Key future work to further develop h-IFS includes understanding the

effect of particle size on scattering intensity spectrum and how to extract a particle's refractive index based on its h-IFS spectrum.

Chapter 4: Summary and Future Experiments

In summary, we demonstrated the use of correlative IFS and fluorescence microscopy to investigate particle size and surface properties of protein aggregates on a single particle scale. Using fluorescent labels that target different protein aggregate surface structures, we investigated how Fc domain and hydrophobic group presentation were affected by aggregate size. We demonstrated the utility of h-IFS to measure the optical scattering intensity spectra of individual protein aggregates.

4.1 Key Findings

- Smaller monoclonal antibody aggregates of ~100 nm showed higher surface concentrations of Fc domains and hydrophobic regions.
- h-IFS microscopy enables the measuring individual scattering spectra of protein aggregates, which showed a range of spectral shapes and peak scattering wavelength that depended on particle size.

4.2 Future Experiments

4.2.1 Correlative IFS and Fluorescence Microscopy

To further support the results from experiments in this thesis, future work should focus on performing additional ensemble fluorescence measurements to confirm the single particle IFS and fluorescence microscopy measurements. The bulk fluorescence and absorbance of labeled protein aggregate samples filtered into multiple size ranges can be measured with a multi-mode plate reader. Additionally, we can repeat our multiscale imaging experiments with different fluorescent labels to investigate other protein

aggregate surface attributes. For example, since we have already used anti-IgG1 Fc secondary antibodies, we can also use anti-IgG1 Fab secondary antibody can be used to investigate Fab presentation on the aggregate surface, which will determine whether protein aggregates remain efficacious against disease targets. Another possible future experiment would test the ability of correlative IFS and fluorescence microscopy to distinguish protein aggregates based on surface structure concentration differences. The surface Fc domain concentration can be artificially reduced by incubation with Protein A (which binds strongly to antibody Fc regions). Then, the Protein A-bound aggregate sample can be mixed with native aggregates and labeled with anti-IgG1 Fc secondary antibodies. The resulting IFS-fluorescence intensity correlation can be examined for distinct particle populations.

We can also repeat our multiscale imaging experiments using the same fluorescent labels, but with protein aggregate sample produced by other stresses. Instead of stirring NISTmAb samples, aggregates can be formed by holding at high temperatures or pH for an extended period. Alternatively, the protein solution could be stirred under different conditions. For example, they can be stirred in a metal container instead of glass. The goal is to extend our multiscale IFS-fluorescence microscopy method to characterize multiple types of protein aggregates formed during typical biopharmaceutical processes and determine whether the type of stress has any effect on the surface structure of the protein aggregates.

Lastly, inherent noisiness of IFS-fluorescence intensity correlations at larger particle sizes (~500-1000 nm) limits the characterizable size range of our multiscale imaging method. The fluorescence labeling procedure should be modified for future

experiments to better eliminate non-specific binding. For example, protein aggregate and label incubation can be done in solution instead of on the IFS sensor surface. Then, a dialysis step can be added to remove excess label from the labeled protein aggregate solution before depositing on the IFS sensor.

4.2.2 h-IFS Microscopy

Future work will establish a robust method to classify particle composition based on their h-IFS scattering spectra. First, the effect of particle size on scattering intensity spectra needs to be better understood. We can prepare polydisperse samples model nanoparticles, for example polystyrene, and measure their scattering intensity spectra using h-IFS. Samples of known refractive index and size can be measured with h-IFS to establish calibration curves to classify particles. Once we have developed a model to extract refractive index from scattering intensity spectra, we need to validate our method using mixtures of nanoparticle samples. For example, monodisperse solutions of iron oxide, polystyrene, and silicon dioxide can be prepared to simulate the typical metal, plastic, and glass contaminants in biologics. Silicone oil is a common contaminant in biologics, so future experiments should focus on identifying silicone oil droplets mixed with protein aggregates.

Appendix

A.1 MATLAB Code to Process Background IFS Images

```
% This script process the background IFS image for background
subtraction.
clear, close all
clc
% Background
[FileName_b, PathName_b] = uigetfile('*.tif','stack of background
images to be processed','Multiselect','off');
%% Background images
focalheights = 20; % Number of focal heights in the z-stack
frames = 35; % Number of time points per focal height
num_images = focalheights*frames;
%%

TifLink_b = Tiff(FileName_b);

    for j = 1:focalheights

        for i = j:focalheights:num_images-focalheights+j

            TifLink_b.setDirectory(i)
            I_b = TifLink_b.read();
            Isum_b(:,:,(i-j)/focalheights+1) = I_b(:,:,1);

        end

    I_ave_b(:,:,j) = uint16(mean(double(Isum_b),3));

    end

TifLink_b.close();
%%
save(['backsub_IFStracked_',FileName_b(1:end-4)])
```

A.2 MATLAB Code to Process and Analyze IFS Images

```
%% This script opens a stack of IFS images for processing. Background
subtraction requires a porcessed background .mat file
% from background_processing_tiff.m

clear, close all
clc
%% Background
[FileName_b, PathName_b] = uigetfile('*.mat','stack of background
images','Multiselect','off');
%%
background = load(FileName_b,'I_ave_b'); % Load background image
processed in "background_processing_tiff.m"
I_ave_b = background.I_ave_b;
```

```
focalheights = 20; % Number of focal heights in the z-stack
frames = 35;
num_images = focalheights*frames;


%% IFS
[FileName, PathName] = uigetfile('*.tif','stack of sample images to be
processed','Multiselect','off');
%%
TifLink = Tiff(FileName, 'r');

%% for IFS image
% Isum = zeros(nimage,mimage,focalheights,'uint16');

for j = 1:focalheights

    for i = j:focalheights:num_images-focalheights+j

        TifLink.setDirectory(i)
        I = TifLink.read();
        Isum(:,:,(i-j)/focalheights+1) = I(:,:,1);
    end

    I_ave(:,:,j) = uint16(mean(double(Isum),3));

end

TifLink.close();

I_test = (double(I_ave_b)./double(I_ave));

%% 16bit

I_test_divide_16bit = uint16(65536 * mat2gray(I_test));

for i = 1:focalheights

    I_test_background_16bit = medfilt2(I_test_divide_16bit(:,:,i),[50
50]);

end

Ifinal_filter_16bit = (uint16((double(I_test_divide_16bit) -
double(I_test_background_16bit))));

%% 8bit

I_test_divide_8bit = uint8(255 * mat2gray(I_test));

for i = 1:focalheights
```

```
    I_test_background_8bit = medfilt2(I_test_divide_8bit(:,:,i),[50
50]);

end

Ifinal_filter_8bit = (uint8((double(I_test_divide_8bit) -
double(I_test_background_8bit))));

%% Tracking max pixel intensity

areamax = 100;
areamin = 3;
data =
struct('NumCirc',[],'Total',[],'Stats',[],'PixelList',[],'Intensity',[]
,'MaxIntensity',[]);
T = 0.4; % image threshold (will need to change when illumination
changes)
N = 1; %noise level for image analysis

I = Ifinal_filter_8bit;

i = 11; % Manually focused frame from z-stack
Infocus = imadjust(I(:,:,i));
bw = im2bw(imadjust(I(:,:,i)),T); %threshold image
bw2 = bwareaopen(bw,N); %elimates noise from image, anything below N
bw3 = imfill(bw2,'holes'); % fills in holes
bw4 = imclearborder(bw3); % clear objects from the border
L = bwlabel(bw4);
stats =
regionprops(L,'Centroid','Area','Eccentricity','PixelList'); %determine
s statistics of image analysis

  %disciminating function
    circind = find([stats.Area]<areamax & [stats.Area]>areamin &
[stats.Eccentricity] < 0.8);
    notcircind = setxor(circind,1:length(stats));

    data.Total = length(stats);
    data.NumCirc = length(circind);
    data.Stats = stats(circind);

    bwcirc = ismember(L,circind);
    bwnotcirc = ismember(L,notcircind);

    Bcirc = bwboundaries(bwcirc,'noholes');
    Bnotcirc = bwboundaries(bwnotcirc,'noholes');


    cla;
    figure(1)
    imshow(Infocus) % or Infocus
    hold on

    for k = 1:length(Bcirc)
```

```
        boundary = Bcirc{k};
        plot(boundary(:,2), boundary(:,1), '-r', 'LineWidth', 1)
    end

    for k = 1:length(Bnotcirc)
        boundary = Bnotcirc{k};
        plot(boundary(:,2), boundary(:,1), '-b', 'LineWidth', 1)
    end

    numparticles = length(circind)
%% Extract particles intensities at each focal height

for c = 1:focalheights

    for w = 1:length(data.Stats)

        data.Intensity(w,1:3,c) =
max(impixel(Ifinal_filter_16bit(:,:,c),data.Stats(w).PixelList(:,1)',da
ta.Stats(w).PixelList(:,2)'));

    end
end

for d = 1:length(data.Intensity)
    data.MaxIntensity(d,:) = max(data.Intensity(d,:));
end

%% save data as mat file

save(['IFStracked_',FileName(1:end-4)])
```

A.3 MATLAB Code to Process and Analyze Fluorescence Images

```
%% This script process a fluorescence image, tracks particle positions,
and measures particle intensities
clear, close all
clc
%% Fluorescent images
[FileName, PathName] = uigetfile('*.tif','stack of fluorescent images
to be processed','Multiselect','off');
%%

TifLink_f = Tiff(FileName);


    I_f = TifLink_f.read();
    Isum_f = I_f;

    I_ave_f = uint16(mean(double(Isum_f),3));


TifLink_f.close();
```

```
%%
areamax = 200;
areamin = 1;
data_Fluor =
struct('NumCirc',[],'Total',[],'Stats',[],'PixelList',[],'Intensity',[]
,'MaxIntensity',[]);
T = 0.8; % image threshold (will need to change when illumination
changes)
N = 1; %noise level for image analysis

    i = 11; % Center of z-stack, manually focused
    I = I_ave_f;
%     [X,Y,I2,rect] = imcrop(imadjust(I));
%     I3 = imcrop(I,rect);
%     Iback = medfilt2(I,[150 150]);
%     I4 = imsubtract(I,Iback);
    bw = im2bw(imadjust(I),T); %threshold image
    bw2 = bwareaopen(bw,N); %elimates noise from image, anything below
N
    bw3 = imfill(bw2,'holes'); % fills in holes
    bw4 = imclearborder(bw3); % clear objects from the border
    L_Fluor = bwlabel(bw4);
    stats =
regionprops(L_Fluor,'Centroid','Area','Eccentricity','PixelList','Major
AxisLength','Orientation'); %determines statistics of image analysis
    %         imshow(L)

    %disciminating function
    circind = find([stats.Area]<areamax & [stats.Area]>areamin &
[stats.Eccentricity]<0.8);
    notcircind = setxor(circind,1:length(stats));

    data_Fluor.Total = length(stats);
    data_Fluor.NumCirc = length(circind);
    data_Fluor.Stats = stats(circind);

    % %         plot boundaries
    cla;
    figure(1), imshow(imadjust(I))
    hold on

    bwcirc = ismember(L_Fluor,circind);
    bwnotcirc = ismember(L_Fluor,notcircind);

    Bcirc = bwboundaries(bwcirc,'noholes');
    Bnotcirc = bwboundaries(bwnotcirc,'noholes');


    for k = 1:length(Bcirc)
        boundary = Bcirc{k};
        plot(boundary(:,2), boundary(:,1), '-r', 'LineWidth', 1)
    end

    for k = 1:length(Bnotcirc)
```

```
        boundary = Bnotcirc{k};
        plot(boundary(:,2), boundary(:,1), '-b', 'LineWidth', 1)
    end
    hold off

    numparticles = length(circind)

%% use pixel list to measure intensity


 for w = 1:length(data_Fluor.Stats)

        data_Fluor.Intensity(w,1:3) =
max(impixel(I_ave_f(:,:),data_Fluor.Stats(w).PixelList(:,1)',data_Fluor
.Stats(w).PixelList(:,2)'));

 end

%% Renaming variable for consistency (max intensity was already
measured)
for d = 1:length(data_Fluor.Intensity)
    data_Fluor.MaxIntensity(d,:) = max(data_Fluor.Intensity(d,:));
end



%% save data as mat file
save(['Fluortracked_',FileName(1:end-4)])
```

A.4 MATLAB Code to Correlate IFS and Fluorescence Images

```
%% Measure size for IFS experiments
%Works for files: SEM_40x_backgroundsub and 40x_png
clear, close all
clc

%% Enter filenames of the IFS and fluorescence tracked images
FileName_IFS =
'IFStracked_IFS_10ugml_AF488_IgG_1mgml_NISTmAb_filtered_undiluted_new20
x_6.mat';
FileName_FL =
'Fluortracked_Fluor_10ugml_AF488_IgG_1mgml_NISTmAb_filtered_undiluted_n
ew20x_6.mat';
IFS = load(FileName_IFS,'data');
FL = load(FileName_FL,'data_Fluor');



test_dist_standard = 7; % Distance between IFS and FL images of
particle centroids

correlation_data =
struct('Intensity',[],'Area',[],'MajorAxisLength',[],'CentroidIFS',[],'
CentroidFL',[],'Orientation',[]);
```

```
for j = 1:length(IFS.data.Stats) %loop through all iscat particles
%     j
    for k = 1:length(FL.data_Fluor.Stats) %find accompanying particle
in SEM
%         k %2.66 for 100x, 2.35 for 40x, 2.0 for new 40x image
        test_dist = sqrt((IFS.data.Stats(j).Centroid(1,1) -
FL.data_Fluor.Stats(k).Centroid(1,1))^2 +
(IFS.data.Stats(j).Centroid(1,2) -
FL.data_Fluor.Stats(k).Centroid(1,2))^2);

        if test_dist < test_dist_standard % 5 - 10 is a good starting
range, may need to be adjusted based on image magnification, particle
concentration, if you see error or very few data points, increase
slightly

            correlation_data.Intensity(j,1:2) =
[FL.data_Fluor.MaxIntensity(k) (IFS.data.MaxIntensity(j))];

            correlation_data.CentroidIFS(j,1:2) =
[IFS.data.Stats(j).Centroid(1,1)*3.12
IFS.data.Stats(j).Centroid(1,2)*3.12];
            correlation_data.CentroidFL(j,1:2) =
[FL.data_Fluor.Stats(k).Centroid(1,1)
FL.data_Fluor.Stats(k).Centroid(1,2)];
            correlation_data.eccentricity(j,1:2) =
[FL.data_Fluor.Stats(k).Eccentricity IFS.data.Stats(j).Eccentricity];
%             correlation_data.Orientation(j,1:2) =
[data_SEM.Stats(k).Orientation data.Stats(j).Orientation];

        else

        end
    end
end
%%
num_matches = correlation_data.Intensity;
num_matches(matches==0) = [];
num_matches = length(matches)/2

%% Save

save(['Correlated_z11_',FileName_IFS(12:end-4)])
```

A.5 MATLAB Code to Process background h-IFS Images

```
clear, clc
%% Processes h-IFS image with 7 wavelengths
% Background
[FileName_b, PathName_b] = uigetfile('*.tif','stack of background
images to be processed','Multiselect','off');
%% for background image
iminfo_b = imfinfo([PathName_b,FileName_b]); % REPLACE MOVINFO WITH
IMINFO AND VIDEOREADER WITH TIFFLIB
```

```
mimage = iminfo_b.Width; % REPLACE WITH IMINFO
nimage = iminfo_b.Height;
% Update these if number of time points, focal heights, or wavelengths
changes
time = 25;
focalheights = 15;
channels = 7;
num_images = time*focalheights*channels;

TifLink_b = Tiff(FileName_b);

I_sum_b = zeros(mimage,nimage,time,'uint16');
I_ave_b = zeros(mimage,nimage,focalheights,channels,'uint16');

    for i = 1:channels % each channel
        for j = 1:focalheights % each focal height
            for k = (i-
1)*focalheights+j:focalheights*channels:num_images-
focalheights*channels+focalheights*(i-1)+j % each time point
                TifLink_b.setDirectory(k)
                I_b = TifLink_b.read();
                I_sum_b(:,:,((k-j)-(i-
1)*focalheights)/(focalheights*channels)+1) = I_b(:,:,1);
            end
        I_ave_b(:,:,j,i) = uint16(mean(double(I_sum_b),3));
        end
    end
TifLink_b.close();
%% save data as mat file

save(['backsub_IFStracked_',FileName_b(1:end-4)],'I_ave_b')
```

A.6 MATLAB Code to Process and Analyze h-IFS Images

```
clear, clc
%% This script processes an h-IFS .tiff image with 7 wavelengths
(channels), time-averaging, and focal height series. Measures and
extracts the max intensities at each wavelength.
% Background
[FileName_b, PathName_b] = uigetfile('*.mat','stack of background
images to be processed','Multiselect','off');
%% for background image
% Update these if number of time points, focal heights, or wavelengths
changes
time = 25;
focalheights = 15;
channels = 7;
num_images = time*focalheights*channels;

background = load(FileName_b,'I_ave_b'); % Load background image
processed in "background_processing_tiff.m"
I_ave_b = background.I_ave_b;
```

```
%% IFS
[FileName, PathName] = uigetfile('*.tif','stack of sample images to be
processed','Multiselect','off');
%%
TifLink = Tiff(FileName, 'r');

%% for IFS image
% Isum = zeros(nimage,mimage,focalheights,'uint16');
I_sum = zeros(mimage,nimage,time,'uint16');
I_ave = zeros(mimage,nimage,focalheights,channels);


    for i = 1:channels % each channel
        for j = 1:focalheights % each focal height
            for k = (i-
1)*focalheights+j:focalheights*channels:num_images-
focalheights*channels+focalheights*(i-1)+j % each time point
                TifLink.setDirectory(k)
                I = TifLink.read();
                I_sum(:,:,((k-j)-(i-
1)*focalheights)/(focalheights*channels)+1) = I(:,:,1);
            end
        I_ave(:,:,j,i) = uint16(mean(double(I_sum),3),'uint16');
        end
    end

TifLink.close();

%%
I_test = (double(I_ave_b)./double(I_ave));

%% 16 bit

I_test_divide_16bit = uint16(65536 * mat2gray(I_test));

for i = 1:7
    for    j = 1:focalheights
    I_test_background_16bit(:,:,j,i) =
medfilt2(I_test_divide_16bit(:,:,j,i),[50 50]);
    end
end

Ifinal_filter_16bit = (uint16((double(I_test_divide_16bit) -
double(I_test_background_16bit))));

%% 8bit

I_test_divide_8bit = uint8(255 * mat2gray(I_test));

for i = 1:7
    for    j = 1:focalheights
        I_test_background_8bit(:,:,j,i) =
medfilt2(I_test_divide_8bit(:,:,j,i),[50 50]);
    end
```

```
end

Ifinal_filter_8bit = (uint8((double(I_test_divide_8bit) -
double(I_test_background_8bit))));

%%

%% Tracking max pixel intensity
% Perform tracking on channel 5, in focus z-slice 8
i = 5; % channel 5
j = 8; % zslice 8
areamax = 100;
areamin = 5;
data =
struct('NumCirc',[],'Total',[],'Stats',[],'PixelList',[],'Intensity',[]
,'MaxIntensity_focalheight',[],'MaxIntensity_wavelength',[]);
T = 0.4; % image threshold (will need to change when illumination
changes)
N = 1; %noise level for image analysis

% for i = 1:length(FileName)
I = Ifinal_filter_8bit;


% [X,Y,I2,rect] = imcrop((I));
% I3 = imcrop(I,rect);
Infocus = imadjust(I(:,:,j,i));
bw = im2bw(imadjust(I(:,:,j,i)),T); %threshold image
bw2 = bwareaopen(bw,N); %elimates noise from image, anything below N
bw3 = imfill(bw2,'holes'); % fills in holes
bw4 = imclearborder(bw3); % clear objects from the border
L = bwlabel(bw4);
stats =
regionprops(L,'Centroid','Area','Eccentricity','PixelList'); %determine
s statistics of image analysis

  %disciminating function
    circind = find([stats.Area]<areamax & [stats.Area]>areamin &
[stats.Eccentricity] < 0.7);
    notcircind = setxor(circind,1:length(stats));

    data.Total = length(stats);
    data.NumCirc = length(circind);
    data.Stats = stats(circind);

    bwcirc = ismember(L,circind);
    bwnotcirc = ismember(L,notcircind);

    Bcirc = bwboundaries(bwcirc,'noholes');
    Bnotcirc = bwboundaries(bwnotcirc,'noholes');


    numparticles = length(circind)
```

```
%%
    cla;
    figure(1)
    imshow(Infocus) % or Infocus
    hold on

    for k = 1:length(Bcirc)
        boundary = Bcirc{k};
        plot(boundary(:,2), boundary(:,1), '-r', 'LineWidth', 1)
    end

    for k = 1:length(Bnotcirc)
        boundary = Bnotcirc{k};
        plot(boundary(:,2), boundary(:,1), '-b', 'LineWidth', 1)
    end
%                 pause
%                 close all

    %
%% Apply xy shift correction measured from ImageJ
% Using channel 5 as a reference, example correction 1 = channel 5(xy)
- channel 1(xy)
% index 1-4 are corrections to channels 1-4; correction to channel 5 is
always 0,
% then 6 and 7 are corrections
% The pixel xy shift was manually measured in ImageJ at z=8

xy_corr(1,:) = [-1 -4];
xy_corr(2,:) = [0 -3];
xy_corr(3,:) = [0 -2];
xy_corr(4,:) = [0 -1];
xy_corr(5,:) = [0 0];
xy_corr(6,:) = [0 1];
xy_corr(7,:) = [0 1];

%% use pixel list to measure intensity at each wavelength, save in
data.Intensity
% Find the intensity of each particle defined by the pixel list at each
% focal height and channel
for i = 1:channels
    for j = 1:focalheights
         for m = 1:length(data.Stats)
            data.Intensity(m,1:3,j,i) =
max(impixel(Ifinal_filter_16bit(:,:,j,i),data.Stats(m).PixelList(:,1)'+
xy_corr(i,1),data.Stats(m).PixelList(:,2)'+xy_corr(i,2)));
%          intensity1{i} = intensity(:,1);

         end
    end
end
% For each channel, find the max intensity of a particle between all
focal heights
for i = 1:channels
    for m = 1:length(data.Intensity)
        data.MaxIntensity_focalheight(m,1,i) =
max(data.Intensity(m,1,:,i));
```

```
    end
end
% Find which wavelength the peak intensity is for each particle, column
1
% is the peak intensity, column 2 is the channel where that peak
intensity
% was found (which corresponds to wavelenghth)
for m = 1:length(data.Intensity)

[data.MaxIntensity_wavelength(m,1),data.MaxIntensity_wavelength(m,2)] =
max(data.MaxIntensity_focalheight(m,1,:));
end

%% Map channels to wavelength in 3rd column of data

data.MaxIntensity_wavelength(:,3) =
wavelength(data.MaxIntensity_wavelength(:,2));

save(['IFStracked_',FileName(1:end-4)])
```

Bibliography

1. Ecker, D. M. MAb Products: Market Trends and Projections. https://bioprocessintl.com/business/economics/the-market-for-therapeutic-mab-products/ (accessed March 23).
2. Reichert, J. M., Marketed therapeutic antibodies compendium. *mAbs* **2012,** *4* (3), 413-5.
3. Ecker, D. M.; Jones, S. D.; Levine, H. L., The therapeutic monoclonal antibody market. *mAbs* **2015,** *7* (1), 9-14.
4. Nicholson, L. B., The immune system. *Essays Biochem* **2016,** *60* (3), 275-301.
5. BxCell Antibody Structure. https://bxcell.com/antibody-structure/ (accessed Mar 25).
6. Chiu, M. L.; Goulet, D. R.; Teplyakov, A.; Gilliland, G. L., Antibody Structure and Function: The Basis for Engineering Therapeutics. *Antibodies (Basel)* **2019,** *8* (4), 55.
7. Chaplin, D. D., Overview of the immune response. *J Allergy Clin Immunol* **2010,** *125* (2 Suppl 2), S3-S23.
8. An Introduction to Antibodies: Antigens, Epitopes and Antibodies. https://www.sigmaaldrich.com/technical-documents/articles/biology/antigens-epitopes-antibodies.html (accessed Mar 25).
9. Liu, J. K. H., The history of monoclonal antibody development - Progress, remaining challenges and future innovations. *Ann Med Surg (Lond)* **2014,** *3* (4), 113-116.
10. Li, J.; Zhu, Z., Research and development of next generation of antibody-based therapeutics. *Acta Pharmacol Sin* **2010,** *31* (9), 1198-1207.
11. Nelson, A. L.; Dhimolea, E.; Reichert, J. M., Development trends for human monoclonal antibody therapeutics. *Nature Reviews. Drug Discovery* **2010,** *9* (10), 767-74.
12. Hammers, C. M.; Stanley, J. R., Antibody phage display: technique and applications. *J Invest Dermatol* **2014,** *134* (2), 1-5.
13. Gronemeyer, P.; Ditz, R.; Strube, J., Trends in Upstream and Downstream Process Development for Antibody Manufacturing. *Bioengineering* **2014,** *1* (4).
14. Jain, E.; Kumar, A., Upstream processes in antibody production: evaluation of critical parameters. *Biotechnology Advances* **2008,** *26* (1), 46-72.
15. Shukla, A. A.; Thömmes, J., Recent advances in large-scale production of monoclonal antibodies and related proteins. *Trends in Biotechnology* **2010,** *28* (5), 253-261.
16. Carpenter, J. F.; Randolph Tw Fau - Jiskoot, W.; Jiskoot W Fau - Crommelin, D. J. A.; Crommelin Dj Fau - Middaugh, C. R.; Middaugh Cr Fau - Winter, G.; Winter, G., Potential inaccurate quantitation and sizing of protein aggregates by size exclusion chromatography: essential need to use orthogonal methods to assure the quality of therapeutic protein products. (1520-6017 (Electronic)).
17. Carpenter, J. F.; Randolph, T. W.; Jiskoot, W.; Crommelin, D. J.; Middaugh, C. R.; Winter, G.; Fan, Y. X.; Kirshner, S.; Verthelyi, D.; Kozlowski, S.; Clouse, K. A.; Swann, P. G.; Rosenberg, A.; Cherney, B., Overlooking subvisible particles in therapeutic protein products: gaps that may compromise product quality. *Journal of Pharmaceutical Sciences* **2009,** *98* (4), 1201-5.

18. Bansal, R.; Dash, R.; Rathore, A. S., Impact of mAb Aggregation on Its Biological Activity: Rituximab as a Case Study. *Journal of Pharmaceutical Sciences* **2020,** *109* (9), 2684-2698.
19. Casadevall, N.; Nataf, J.; Viron, B.; Kolta, A.; Kiladjian, J. J.; Martin-Dupont, P.; Michaud, P.; Papo, T.; Ugo, V.; Teyssandier, I.; Varet, B.; Mayeux, P., Pure red-cell aplasia and antierythropoietin antibodies in patients treated with recombinant erythropoietin. *The New England journal of medicine* **2002,** *346* (7), 469-75.
20. Narhi, L. O.; Schmit, J.; Bechtold-Peters, K.; Sharma, D., Classification of Protein Aggregates¹. *Journal of Pharmaceutical Sciences* **2012,** *101* (2), 493-498.
21. Kijanka, G.; Bee, J. S.; Korman, S. A.; Wu, Y.; Roskos, L. K.; Schenerman, M. A.; Slütter, B.; Jiskoot, W., Submicron Size Particles of a Murine Monoclonal Antibody Are More Immunogenic Than Soluble Oligomers or Micron Size Particles Upon Subcutaneous Administration in Mice. *Journal of Pharmaceutical Sciences* **2018,** *107* (11), 2847-2859.
22. Nejadnik, M. R.; Randolph, T. W.; Volkin, D. B.; Schöneich, C.; Carpenter, J. F.; Crommelin, D. J. A.; Jiskoot, W., Postproduction Handling and Administration of Protein Pharmaceuticals and Potential Instability Issues. *Journal of Pharmaceutical Sciences* **2018,** *107* (8), 2013-2019.
23. Jiskoot, W.; Nejadnik, M. R.; Sediq, A. S., Potential Issues With the Handling of Biologicals in a Hospital. *Journal of pharmaceutical sciences* **2017,** *106* (6), 1688-1689.
24. Vlieland, N. D.; Gardarsdottir, H.; Bouvy, M. L.; Egberts, T. C. G.; van den Bemt, B. J. F., The majority of patients do not store their biologic disease-modifying antirheumatic drugs within the recommended temperature range. *Rheumatology* **2016,** *55* (4), 704-709.
25. Morris, A. M.; Watzky, M. A.; Finke, R. G., Protein aggregation kinetics, mechanism, and curve-fitting: a review of the literature. *Biochimica et Biophysica Acta* **2009,** *1794* (3), 375-97.
26. Singla, A.; Bansal, R.; Joshi, V.; Rathore, A. S., Aggregation Kinetics for IgG1-Based Monoclonal Antibody Therapeutics. *AAPS J* **2016,** *18* (3), 689-702.
27. Bria, C. R. M.; Jones, J.; Charlesworth, A.; Williams, S. K. R., Probing Submicron Aggregation Kinetics of an IgG Protein by Asymmetrical Flow Field-Flow Fractionation. *Journal of Pharmaceutical Sciences* **2016,** *105* (1), 31-39.
28. Brummitt, R. K.; Nesta, D. P.; Chang, L.; Kroetsch, A. M.; Roberts, C. J., Nonnative aggregation of an IgG1 antibody in acidic conditions, part 2: nucleation and growth kinetics with competing growth mechanisms. *Journal of Pharmaceutical Sciences* **2011,** *100* (6), 2104-19.
29. Rosenberg, A. S., Effects of protein aggregates: an immunologic perspective. *AAPS J* **2006,** *8* (3), E501-7.
30. Moussa, E. M.; Panchal, J. P.; Moorthy, B. S.; Blum, J. S.; Joubert, M. K.; Narhi, L. O.; Topp, E. M., Immunogenicity of Therapeutic Protein Aggregates. *Journal of Pharmaceutical Sciences* **2016,** *105* (2), 417-430.
31. Tada, M.; Aoyama, M.; Ishii-Watabe, A., Fcγ Receptor Activation by Human Monoclonal Antibody Aggregates. *Journal of Pharmaceutical Sciences* **2020,** *109* (1), 576-583.

32. den Engelsman, J.; Garidel, P.; Smulders, R.; Koll, H.; Smith, B.; Bassarab, S.; Seidl, A.; Hainzl, O.; Jiskoot, W., Strategies for the assessment of protein aggregates in pharmaceutical biotech product development. *Pharm Res* **2011,** *28* (4), 920-933.
33. Mahler, H. C.; Friess, W.; Grauschopf, U.; Kiese, S., Protein aggregation: pathways, induction factors and analysis. *Journal of Pharmaceutical Sciences* **2009,** *98* (9), 2909-34.
34. Hong, P.; Koza, S.; Bouvier, E. S. P., Size-Exclusion Chromatography for the Analysis of Protein Biotherapeutics and their Aggregates. *J Liq Chromatogr Relat Technol* **2012,** *35* (20), 2923-2950.
35. Yu, Z.; Reid, J. C.; Yang, Y.-P., Utilizing Dynamic Light Scattering as a Process Analytical Technology for Protein Folding and Aggregation Monitoring in Vaccine Manufacturing. *Journal of Pharmaceutical Sciences* **2013,** *102* (12), 4284-4290.
36. Li, Y.; Lubchenko, V.; Vekilov, P. G., The use of dynamic light scattering and brownian microscopy to characterize protein aggregation. *The Review of Scientific Instruments* **2011,** *82* (5), 053106.
37. Bäuerlein, F. J. B.; Fernández-Busnadiego, R.; Baumeister, W., Investigating the Structure of Neurotoxic Protein Aggregates Inside Cells. *Trends in Cell Biology* **2020,** *30* (12), 951-966.
38. Sung, J. J.; Pardeshi, N. N.; Mulder, A. M.; Mulligan, S. K.; Quispe, J.; On, K.; Carragher, B.; Potter, C. S.; Carpenter, J. F.; Schneemann, A., Transmission electron microscopy as an orthogonal method to characterize protein aggregates. *Journal of Pharmaceutical Sciences* **2015,** *104* (2), 750-759.
39. Panchal, J.; Kotarek, J.; Marszal, E.; Topp, E. M., Analyzing subvisible particles in protein drug products: a comparison of dynamic light scattering (DLS) and resonant mass measurement (RMM). *AAPS J* **2014,** *16* (3), 440-51.
40. Krueger, A. B.; Hadley, J.; Cheney, P. P.; Markova, N.; Carpenter, J. F.; Fradkin, A. H., Application of a Best Practice Approach Using Resonant Mass Measurement for Biotherapeutic Product Characterization. *Journal of Pharmaceutical Sciences* **2019,** *108* (5), 1675-1685.
41. Grabarek, A. D.; Weinbuch, D.; Jiskoot, W.; Hawe, A., Critical Evaluation of Microfluidic Resistive Pulse Sensing for Quantification and Sizing of Nanometer- and Micrometer-Sized Particles in Biopharmaceutical Products. *Journal of Pharmaceutical Sciences* **2019,** *108* (1), 563-573.
42. Barnett, G. V.; Perhacs, J. M.; Das, T. K.; Kar, S. R., Submicron Protein Particle Characterization using Resistive Pulse Sensing and Conventional Light Scattering Based Approaches. *Pharm Res* **2018,** *35* (3), 58.
43. Sharma, D. K.; King, D.; Oma, P.; Merchant, C., Micro-flow imaging: flow microscopy applied to sub-visible particulate analysis in protein formulations. *AAPS J* **2010,** *12* (3), 455-464.
44. Sharma, D. K.; Oma, P.; Pollo, M. J.; Sukumar, M., Quantification and characterization of subvisible proteinaceous particles in opalescent mAb formulations using micro-flow imaging. *Journal of Pharmaceutical Sciences* **2010,** *99* (6), 2628-42.
45. Wong, N. A.; Uchida, N. V.; Dissanayake, T. U.; Patel, M.; Iqbal, M.; Woehl, T. J., Detection and Sizing of Submicron Particles in Biologics With Interferometric Scattering Microscopy. *Journal of Pharmaceutical Sciences* **2020,** *109* (1), 881-890.

46. Young, G.; Kukura, P., Interferometric Scattering Microscopy. *Annual Review of Physical Chemistry* **2019,** *70* (1), 301-322.
47. Taylor, R. W.; Sandoghdar, V., Interferometric Scattering Microscopy: Seeing Single Nanoparticles and Molecules via Rayleigh Scattering. *Nano Letters* **2019,** *19* (8), 4827-4835.
48. Hsieh, C.-L.; Spindler, S.; Ehrig, J.; Sandoghdar, V., Tracking Single Particles on Supported Lipid Membranes: Multimobility Diffusion and Nanoscopic Confinement. *The Journal of Physical Chemistry B* **2014,** *118* (6), 1545-1554.
49. Aoyama, M.; Tada, M.; Ishii-Watabe, A., A Cell-Based Reporter Assay Measuring the Activation of Fc Gamma Receptors Induced by Therapeutic Monoclonal Antibodies. In *Human Monoclonal Antibodies: Methods and Protocols*, Steinitz, M., Ed. Springer New York: New York, NY, 2019; pp 423-429.
50. Ratanji, K. D.; Derrick, J. P.; Dearman, R. J.; Kimber, I., Immunogenicity of therapeutic proteins: influence of aggregation. *Journal of Immunotoxicology* **2014,** *11* (2), 99-109.
51. Joubert, M. K.; Hokom, M.; Eakin, C.; Zhou, L.; Deshpande, M.; Baker, M. P.; Goletz, T. J.; Kerwin, B. A.; Chirmule, N.; Narhi, L. O.; Jawa, V., Highly Aggregated Antibody Therapeutics Can Enhance the in Vitro Innate and Late-stage T-cell Immune Responses. *Journal of Biological Chemistry* **2012,** *287* (30), 25266-25279.
52. Kumar, S.; Mitchell, M. A.; Rup, B.; Singh, S. K., Relationship Between Potential Aggregation-Prone Regions and HLA-DR-Binding T-Cell Immune Epitopes: Implications for Rational Design of Novel and Follow-on Therapeutic Antibodies. *Journal of Pharmaceutical Sciences* **2012,** *101* (8), 2686-2701.
53. Schiel, J. E.; Turner, A.; Mouchahoir, T.; Yandrofski, K.; Telikepalli, S.; King, J.; DeRose, P.; Ripple, D.; Phinney, K., The NISTmAb Reference Material 8671 value assignment, homogeneity, and stability. *Analytical and Bioanalytical Chemistry* **2018,** *410* (8), 2127-2139.
54. NIST Monoclonal Antibody Reference Material 8671. https://www.nist.gov/programs-projects/nist-monoclonal-antibody-reference-material-8671 (accessed Mar 24).
55. Scherr, S. M.; Daaboul, G. G.; Trueb, J.; Sevenler, D.; Fawcett, H.; Goldberg, B.; Connor, J. H.; Ünlü, M. S., Real-Time Capture and Visualization of Individual Viruses in Complex Media. *ACS nano* **2016,** *10* (2), 2827-33.
56. Avci, O.; Campana, M. I.; Yurdakul, C.; Selim Ünlü, M., Pupil function engineering for enhanced nanoparticle visibility in wide-field interferometric microscopy. *Optica* **2017,** *4* (2), 247-254.
57. Mayerhöfer, T. G.; Pipa, A. V.; Popp, J., Beer's Law-Why Integrated Absorbance Depends Linearly on Concentration. *Chemphyschem* **2019,** *20* (21), 2748-2753.
58. Burry, R. W., Controls for immunocytochemistry: an update. *J Histochem Cytochem* **2011,** *59* (1), 6-12.
59. Sediq, A. S.; van Duijvenvoorde, R. B.; Jiskoot, W.; Nejadnik, M. R., No Touching! Abrasion of Adsorbed Protein Is the Root Cause of Subvisible Particle Formation During Stirring. *Journal of Pharmaceutical Sciences* **2016,** *105* (2), 519-529.
60. Wang, X.; Wang, Y.; Xu, H.; Shan, H.; Lu, J. R., Dynamic adsorption of monoclonal antibody layers on hydrophilic silica surface: A combined study by

spectroscopic ellipsometry and AFM. *Journal of Colloid and Interface Science* **2008,** *323* (1), 18-25.
61. Wiseman, M. E.; Frank, C. W., Antibody Adsorption and Orientation on Hydrophobic Surfaces. *Langmuir* **2012,** *28* (3), 1765-1774.
62. Chi, E. Y.; Krishnan, S.; Randolph, T. W.; Carpenter, J. F., Physical stability of proteins in aqueous solution: mechanism and driving forces in nonnative protein aggregation. *Pharm Res* **2003,** *20* (9), 1325-36.
63. Ilinskaya, A. N.; Dobrovolskaia, M. A., Understanding the immunogenicity and antigenicity of nanomaterials: Past, present and future. *Toxicology and Applied Pharmacology* **2016,** *299*, 70-7.
64. Weinbuch, D.; Zölls, S.; Wiggenhorn, M.; Friess, W.; Winter, G.; Jiskoot, W.; Hawe, A., Micro-flow imaging and resonant mass measurement (Archimedes)--complementary methods to quantitatively differentiate protein particles and silicone oil droplets. *Journal of Pharmaceutical Sciences* **2013,** *102* (7), 2152-65.
65. Dixit, N.; Kalonia, D. S., Silicone Oil in Biopharmaceutical Containers: Applications and Recent Concerns. In *Concise Encyclopedia of High Performance Silicones*, 2014; pp 381-394.
66. Liu, J.; Ronk, M.; Fujimori, K.; Lee, H.; Nashed-Samuel, Y., Analysis of Silicone Oil in Prefilled Syringes and Biopharmaceutical Drug Products Using High-Performance Liquid Chromatography. *AAPS PharmSciTech* **2021,** *22* (2), 75.
67. Strehl, R.; Rombach-Riegraf, V.; Diez, M.; Egodage, K.; Bluemel, M.; Jeschke, M.; Koulov, A. V., Discrimination between silicone oil droplets and protein aggregates in biopharmaceuticals: a novel multiparametric image filter for sub-visible particles in microflow imaging analysis. *Pharm Res* **2012,** *29* (2), 594-602.
68. Zhou, S.; Schöneich, C.; Singh, S. K., Biologics formulation factors affecting metal leachables from stainless steel. *AAPS PharmSciTech* **2011,** *12* (1), 411-21.
69. Bee, J. S.; Nelson, S. A.; Freund, E.; Carpenter, J. F.; Randolph, T. W., Precipitation of a monoclonal antibody by soluble tungsten. *Journal of Pharmaceutical Sciences* **2009,** *98* (9), 3290-301.
70. Wang, C.; Zhong, X.; Ruffner, D. B.; Stutt, A.; Philips, L. A.; Ward, M. D.; Grier, D. G., Holographic Characterization of Protein Aggregates. *Journal of Pharmaceutical Sciences* **2016,** *105* (3), 1074-1085.
71. Agrawal, A.; Majdi, J.; Clouse, K. A.; Stantchev, T., Electron-Beam-Lithographed Nanostructures as Reference Materials for Label-Free Scattered-Light Biosensing of Single Filoviruses. *Sensors* **2018,** *18* (6).
72. Daaboul, G. G.; Yurt, A.; Zhang, X.; Hwang, G. M.; Goldberg, B. B.; Ünlü, M. S., High-Throughput Detection and Sizing of Individual Low-Index Nanoparticles and Viruses for Pathogen Identification. *Nano Letters* **2010,** *10* (11), 4727-4731.